RESEARCH ARTICLE

VOLCANICA

Structural controls on magma pathways in the Bora-Baricha-Tullu Moye volcanic system, Main Ethiopian Rift

Amdemichael Zafu Tadesse*[α], Gemechu Bedassa[β], Matthieu Kervyn[γ], Ameha Atnafu Muluneh[δ,ε], Snorri Gudbrandsson[ζ,η], Gezahegn Yirgu[δ], Dereje Ayalew[δ], and Karen Fontijn[α]

[α] Department of Geosciences, Environment and Society, Université libre de Bruxelles (ULB), Belgium.
[β] Department of Geology, Addis Ababa Science and Technology University (AASTU), Addis Ababa, Ethiopia.
[γ] Department of Geography, Vrije Universiteit Brussel (VUB), Belgium.
[δ] School of Earth Sciences, Addis Ababa University (AAU), Ethiopia.
[ε] Helmohltz-centre Potsdam - GFZ German Research Centre for Geosciences, Germany.
[ζ] Reykjavik Geothermal Ltd, Iceland.
[η] TM Geothermal Operations PLC, Ethiopia.

Submitted: 2023-01-20 | Accepted: 2023-08-20 | Published: 2023-10-05

Editor: M. R. James | Typesetter: J. Farquharson

Abstract

The Bora-Baricha-Tullu Moye (BBTM) volcanic complex is located in a transition zone between the central and northern sectors of the Main Ethiopian Rift where tectonic and volcanic features show complex interplays. We mapped and characterised volcanic and tectonic features using high-resolution digital elevation models and performed morphometric and vent spatial distribution analyses. Structural analysis reveals NNE–SSW, NE–SW, and NW–SE trending faults in the region. The dominant post-caldera volcanic landforms are lava domes, pumice cones, scoria cones, maars, obsidian coulees, and lava flows, which have distinct morphological characteristics. Vent elongation and alignment highlight close association between these landforms and the caldera(s) as well as with tectonic structures, suggesting these structures acted as the main magma pathways during the BBTM volcanic system recent eruptions. We estimate that during the entire BBTM volcanic system post-caldera phase a total bulk volume of 10.9 km^3 of material was erupted. This would represent a time-averaged magma flux of 0.05 km^3 ky^{-1} in the BBTM volcanic system.

Keywords: Main Ethiopian Rift; Caldera; Morphometry; Volcanic vent alignment; Magma flux.

1 Introduction

Volcanoes are fed by planar intrusions (i.e. dykes) via crack opening, orienting perpendicular to the least compressive stress [e.g. Rubin 1995]. Hence, the geometry of the magma plumbing system is controlled by regional stress and/or pre-existing structures, and this is partially expressed at the Earth's surface by edifice elongation and vent alignment [e.g. Paulsen and Wilson 2010; Rooney et al. 2011; Le Corvec et al. 2013b]. Spatial distribution and alignment analyses of volcanic vents have been used to understand the influence of tectonic and volcanic (i.e. caldera) structures on magma transportation to the surface [e.g. Tibaldi 1995; Paulsen and Wilson 2010; Le Corvec et al. 2013b; Hutchison et al. 2015; Mazzarini et al. 2016; Hunt et al. 2020]. The morphology of volcanic landforms is also affected by syn-eruptive (e.g. flank slope instabilities, wind direction) and post-eruptive processes (e.g. erosion[Kereszturi and Németh 2012; Kervyn et al. 2012]). Geomorphological analysis of volcanic landforms can help to unravel the interplay between eruption and erosion related processes [e.g. Kereszturi and Németh 2012; Kervyn et al. 2012; Bemis and Ferencz 2017].

In continental rifts, magmatism and tectonics interact at a variety of scales from individual faults and magmatic intrusions to lithospheric structures [Korme et al. 1997; Boccaletti et al. 1998; Casey et al. 2006; Abebe et al. 2007; Rooney et al. 2011; Hutchison et al. 2015; Keir et al. 2015; Maccaferri et al. 2015; Corti et al. 2018a]. The magmatic and tectonic interactions govern rift architecture [e.g. Ebinger and Casey 2001], extensional dynamics [e.g. Daniels et al. 2014], and the location of volcanic vents and edifices [e.g. Acocella et al. 2003; Abebe et al. 2007]. The East African Rift System (EARS) is a prime example of an active continental rift extending from incipient extension to continental break-up [e.g. Corti 2009; Agostini et al. 2011]. The Bora-Baricha-Tullu Moye (BBTM) volcanic system is located mid-way in the Main Ethiopian Rift (MER), at a section where the properties of the lithosphere [e.g. Mackenzie et al. 2005; Maguire et al. 2006; Keranen et al. 2009], visible faults [e.g. Agostini et al. 2011], and eruptions [e.g. Fontijn et al. 2018] drastically change. This tectonic complexity and the high vent density of the BBTM volcanic system provide a good opportunity to study the interplay of magmatism and tectonics to understand the MER evolution [Korme 1999]. The BBTM volcanic system is identified to host abundant faults, fissures, and ring fault networks that are possibly associated with tectonic or caldera collapse processes [Korme 1999].

In this study we report the results of morphometric and geostatistical analyses performed on high-resolution digital elevation models (DEMs) of the BBTM region, integrated with field-based observations of structures and volcanic deposits [Tadesse et al. 2022]. These results are used to improve our understanding of the interaction between magmatism and major volcanic and tectonic structures in the continental rifting setting of the BBTM volcanic system.

* amdemichael.tadesse@ulb.be

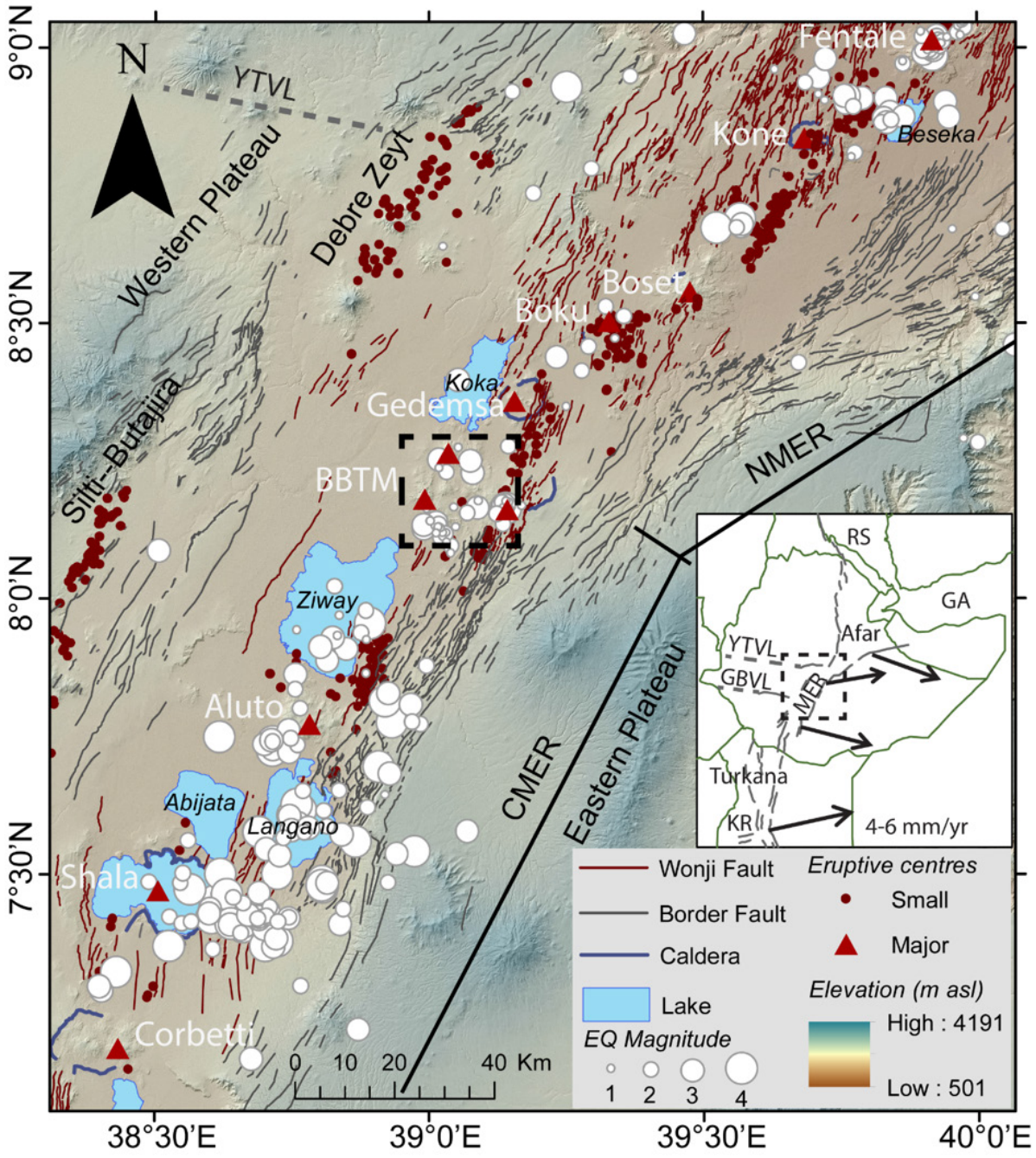

Figure 1: Volcano-tectonic overview map of the Main Ethiopian Rift (MER). The location of the Bora-Baricha-Tullu Moye (BBTM) volcanic system is indicated by a dashed rectangle (for a more detail view, see Figure 2A). The borders of the central (CMER) and northern MER (NMER) sectors are indicated by thick black lines. The Wonji Fault Belt (WFB) is represented by the distribution of Holocene volcanoes and dense faulting on the rift floor. The white circles are earthquake (EQ) data scaled to their magnitudes [Keir et al. 2006]. The MER faults are after Agostini et al. [2011]. Names written in black refer to lakes; those in white to volcanoes. Inset: the Kenyan rift (KR) is connected to the MER by a broadly rifted zone around the Turkana depression. The MER extends northwards to the Afar depression and forms a triple junction with the Gulf of Aden (GA) and Red Sea (RS) rifts. The Yerer-Tullu Welel Volcano Tectonic Lineament (YTVL) and Goba Bonga Volcano Tectonic Lineament (GBVL) are indicated by grey dashed lines. The MER is formed by active extension between the Western and Eastern plateau in an E-W direction (black arrows on the inset map) at a rate of 4–6 mm yr^{-1} [Kogan et al. 2012; Saria et al. 2014]. Note the slight change in spreading direction at the CMER-NMER transition zone.

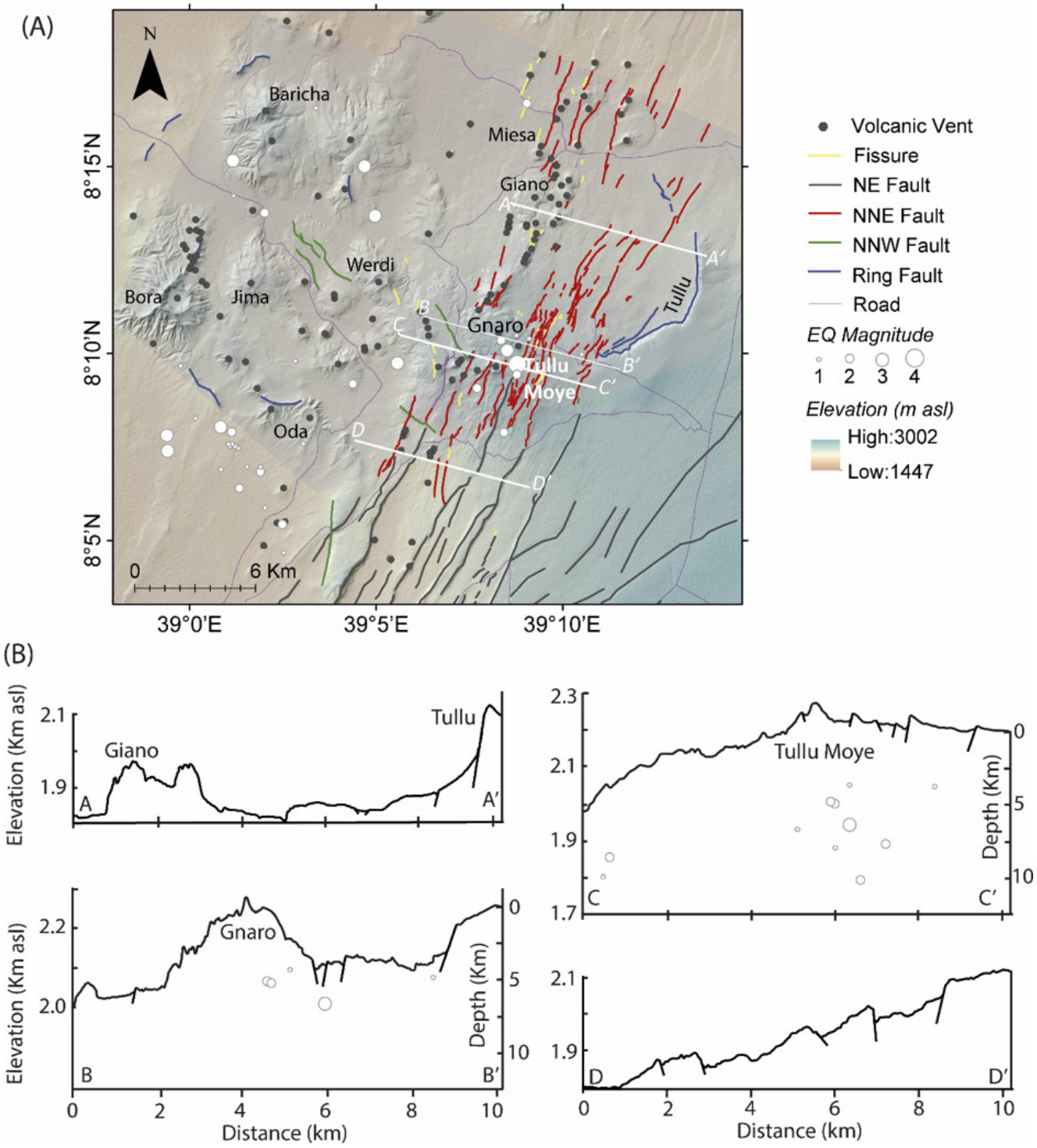

Figure 2: BBTM region [A] structural map and [B] profiles along selected transects indicated in [A]. The structural data is modified after Agostini et al. [2011]. The earthquake (EQ) data are from Keir et al. [2006]. The hill-shade DEM used as a base map is from both the high-resolution LiDAR and ALOS PALSAR data. The profiles have 10× vertical exaggeration.

2 Regional volcano-tectonic setting

The MER accommodates the separation of the Nubian and Somalian plates in the northern part of the EARS at an extension rate of ~4–6 mm yr^{-1} in an E–W direction [Figure 1, e.g. Kogan et al. 2012; Saria et al. 2014]. The MER is bounded by discontinuous boundary faults that have been active since the late Miocene [WoldeGabriel et al. 1990] and strike from NNE–SSW in the south to NE–SW in the north [Corti 2009, and references therein]. Most MER rift sectors (>70 %) are asymmetric with a major boundary fault system in the eastern margin, and with a western margin that is more irregular and marked by minor faulting and monoclines [Corti et al. 2018b]. The recent tectonic and volcanic activity was initiated in the

Quaternary, and predominantly concentrated along faults that are arranged in an en-echelon manner (Wonji Fault Belt, WFB [Mohr 1967; Boccaletti et al. 1998]). The WFB is characterised by recent intense seismicity and volcanic activity [Figure 1; Keir et al. 2006; Abebe et al. 2007]. Overall, the accommodation of lithospheric extension in the MER migrated, through time, from slip along the rift border faults to a focused zone of dyke intrusion and faulting along the rift floor [e.g. Ebinger and Casey 2001; Wolfenden et al. 2004; Casey et al. 2006; Muluneh et al. 2020].

The MER is subdivided into three sectors, depending on the onset and characteristics of rifting: Northern MER (NMER), Central MER (CMER), and Southern MER (SMER). These sectors exhibit different rift trends, fault patterns, lithospheric thicknesses, and strain accommodation mechanisms [Figure 1, e.g. WoldeGabriel et al. 1990; Bonini et al. 2005; Corti 2009; Keir et al. 2015; Muluneh et al. 2017]. The NMER shows well-developed axial and rift border faults trending NNE–SSW and NE–SW, respectively [e.g. Boccaletti et al. 1998; Ebinger and Casey 2001]. The border faults in the NMER have large vertical offsets (>100 m) accommodating tectonic deformation since the Mio-Pliocene (post-11 Ma [Boccaletti et al. 1998]). The WFB is active in the NMER since 2 Ma, and is characterised by a set of closely spaced faults and magmatic centres that jointly accommodate the ongoing deformation [e.g. Boccaletti et al. 1998; Ebinger and Casey 2001]. Geophysical data suggest strong crustal thinning and lithospheric modification beneath the WFB via dyking and normal faulting [Keir et al. 2006; Keranen and Klemperer 2008].

In the CMER, the border faults accommodate extension with subordinate activity from the rift floor faults [e.g. Corti et al. 2020]. In the southern MER, strain is localised in a very narrow zone [e.g. Kogan et al. 2012]; however, broadly distributed deformation is evidenced by surface geology [e.g. Ebinger et al. 1993; Agostini et al. 2011, Figure 1]. The border faults were initiated during the Late Miocene-Pliocene (post-5–8 Ma [WoldeGabriel et al. 1990; Bonini et al. 2005; Abebe et al. 2010]) in the CMER and during the Early Miocene in the SMER (~18 Ma [WoldeGabriel et al. 1990; Ebinger et al. 1993]). In the CMER the WFB faults are mostly localised near the eastern rift margins, whereas the western margin is characterised by volcanic belts with no surface expression of faulting that extend from Silti-Butajira to Debre Zeyt [e.g. WoldeGabriel et al. 1990; Rooney et al. 2007; 2011].

The along-axis variations of rift-related deformation in the different MER sectors is interpreted as a reflection of a transition from early continental rifting in the SMER to mature rifting in the NMER [e.g. Ebinger and Casey 2001; Keir et al. 2006; Corti 2009]. Additionally, the crustal thickness increases from 19–25 km in Afar to ~35–40 km in SMER [Mackenzie et al. 2005; Maguire et al. 2006; Keranen et al. 2009]. Seismic tomographic imaging across the MER confirms strong variations in crust/lithosphere modification and maturity of the magmatic system towards the north [e.g. Keranen and Klemperer 2008]. Moreover, the tectonic and magmatic activity in the MER is further controlled by pre-existing regional E–W or WNW–ESE trending lithospheric heterogeneity [e.g. Bonini et al. 2005; Keranen and Klemperer 2008; Keranen et al. 2009; Corti et al. 2022; Benvenuti et al. 2023]. This heterogeneity corresponds to transfer zones between adjacent segments or (weakened) structures such as the Yere-Tullu Wellel Volcanic Lineament (YTVL) and the Goba-Bonga Volcano Tectonic Lineament (GBVL), almost orthogonal to the general trend of the MER [Figure 1; e.g. Bonini et al. 2005; Keranen and Klemperer 2008; Abebe et al. 2010; Abebe Adhana 2014; Corti et al. 2018a; 2022; Benvenuti et al. 2023]. On a more local scale, the reactivation of pre-existing structures has influenced caldera architecture and the distribution of post-caldera vents (e.g. Corbetti volcano [Acocella et al. 2003; Corti et al. 2018a; Hunt et al. 2019; Maestrelli et al. 2021; Benvenuti et al. 2023]).

The Quaternary volcanic activity has been focused in the axial part of the MER [e.g. WoldeGabriel et al. 1990]. The volcanism is typically bimodal in composition with silicic peralkaline and basaltic products but very few to no intermediate compositions [WoldeGabriel et al. 1990; Tadesse et al. 2019; 2023]. The silicic peralkaline products are mainly associated with regularlyspaced central volcanoes (i.e. Corbetti, Shala, Aluto, BBTM, Gedemsa, Boku, Boset, Kone and Fentale; Figure 1), usually hosting elliptical summit calderas [Ebinger and Casey 2001; Acocella et al. 2003]. The basalts are usually associated with distributed monogenetic vents and/or fissure-fed lavas within or away from the main silicic centres [Ebinger and Casey 2001].

3 Bora-Baricha-Tullu Moye geology

The Bora-Baricha-Tullu Moye (BBTM) volcanic system is located in the transition zone between the NMER and the CMER where the general trend of the MER changes from NE–SW to NNE–SSW [Figure 1 Corti 2009; Agostini et al. 2011]. The pre-BBTM volcanism is represented by older volcanic rocks such as ignimbrites (1.58 ± 0.2 Ma) and basalts (0.44–0.61 ± 0.05 Ma) [WoldeGabriel et al. 1990; Boccaletti et al. 1998; Tadesse et al. 2023]. At least two caldera-forming eruptions have occurred in the BBTM volcanic system, the most recent one dated around 107.7 ± 8.8 ka [Tadesse et al. 2022]. During the post-caldera phase, both explosive and effusive eruptions occurred from several major and small eruptive centres across the complex [Di Paola 1972; Abebe et al. 1998; Korme 1999]. The major eruptive centres are polygenetic and predominantly composed of silicic pyroclastic products (e.g. Baricha, Bora, Werdi, Oda and Tullu Moye; Figures 2 and 3) or silicic lava domes (e.g. Jima [Fontijn et al. 2018; Tadesse et al. 2022]). The small eruptive centres are mostly thought to be monogenetic and predominantly concentrated in the central and eastern parts of the volcanic complex characterised by scoria cones, lava domes and obsidian coulees [e.g. Di Paola 1972; Tadesse et al. 2023]. In addition to pyroclastic deposits and lava flows, lacustrine deposits are also found in the central and southern parts of the complex [Turdu et al. 1999; Benvenuti et al. 2013; Tadesse et al. 2023]. In general, the eruptive products in the BBTM volcanic system are bimodal in composition, ranging from basalts to peralkaline rhyolites linked by fractional crystallisation with minor crustal contamination [Tadesse et al. 2023].

The BBTM is an active volcanic system with ongoing seismicity [Figures 1 and 2; Keir et al. 2006; Greenfield et al. 2019]

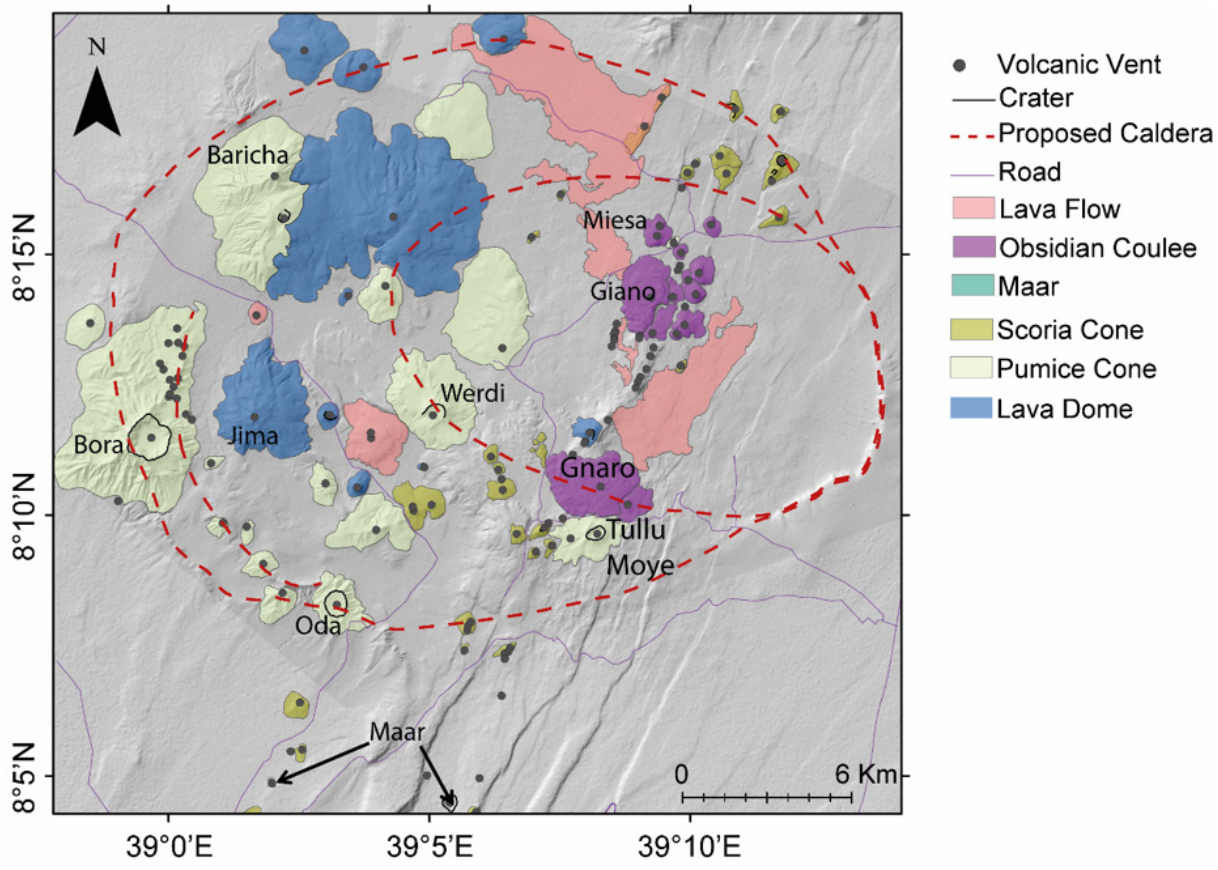

Figure 3: The volcanic landforms map of the BBTM volcanic system. The hill-shade DEM used as a base map is from both the high-resolution LiDAR and ALOS PALSAR data. The volcanic landforms mapped in this study are categorised based on field information and delineated by following breaks in slope.

and surface deformation [Biggs et al. 2011; Albino and Biggs 2021]. The seismicity analysis indicates earthquakes of magnitude M_W<2.7 clustered around the Bora and Tullu Moye edifices [Figure 2; Keir et al. 2006; Greenfield et al. 2019]. Petrological modelling [Tadesse et al. 2023] and magnetotelluric surveys [Samrock et al. 2018; 2021] consistently suggest the presence of magmatic reservoirs at two different depths (~4 km and 7–29 km) under the BBTM volcanic system.

4 Methodology

Volcanic features and vents in the BBTM volcanic system were identified and mapped using data from Digital Elevation Models (DEM) and Google Earth. A high-resolution (2 m) DEM that covers the BBTM volcanic complex was generated from LiDAR data that was acquired by PhotoMap International Inc. in the spring of 2015. The data were delivered in the WGS 1984 UTM zone 37 datum at 2 m grid spacing with 0.2 m accuracy. Details on the LiDAR image processing are discussed by Jonsson [2016]. A DEM derived from ALOS PALSAR sensor data (12.5 m resolution) was used for the part of BBTM volcanic system not covered by the LiDAR and other major volcanoes of the MER. The ALOS PALSAR DEMs were downloaded from the Alaska Satellite Facility*, and are radiometric-terrain corrected. In addition, we used the available studies and 1:50,000 scale geological maps to provide information on the distribution of eruptive products and edifices in the region [Di Paola 1972; Abebe et al. 1998; Korme 1999; Tadesse et al. 2023].

From the DEMs we derived several terrain attributes (e.g. hill-shade, slope, contour) using `ArcGIS`. The different volcanic landforms recognised in the BBTM volcanic system are classified into lava domes, pumice cones, scoria cones, maars, obsidian coulees, and lava flows, following the categories by Hutchison et al. [2015] and Hunt et al. [2019]. The volcanic features on the DEM were visually identified by their relief (negative or positive), shape complexity (circular to elongate), flow morphologies and presence/absence of a crater (Section 5.2). Volcanic features such as pumice cones versus scoria cones and lava domes versus obsidian coulees are sometimes difficult to identify only using the DEM. In that case we used lithological information from the available geological maps. The contacts between different landform features were manually traced at a scale of 1:4000 by following slope breaks on the map of terrain attributes (mainly hill-shade and slope [Grosse et al. 2012]). Additionally, volcanic vent locations were mapped by considering the crater and/or highest peak on the summit region to represent the eruption centre. The preliminary map generated from the DEM observations was complemented by a two-week field campaign in May 2022 to ground-

*https://vertex.daac.asf.alaska.edu/

truth the DEM mapping results in specific areas and to confirm category identification, delimitation and characteristics of the landforms.

The MER fault catalogue from Agostini et al. [2011] was used as a base for fault and lineament mapping. Additional fault structures identified by their vertical offset with the high-resolution DEM were confirmed during the field campaign. The fault and lineament statistics (i.e. length-weighted orientation histogram, length and vertical displacement) were documented from the DEM and field measurements, and analysed using the `RockWorks` and `ArcGIS` software packages.

Morphometric parameters for the mapped volcanic landforms were extracted using the `MORVOLC` algorithm [Grosse et al. 2012]. The inputs for the algorithm are the high-resolution DEM and the manually traced landform boundaries. The `MORVOLC` algorithm uses the landform boundary to generate a 3-D basal surface. This basal surface is generated from fitting the often-irregular landform boundaries using natural, inverse distance weighted and kriging methods. This is employed similarly for all landforms. Then elevation contour lines with an interval of 2 m are generated, and the summit region is defined by tracing the elevation where the edifice starts flattening out [Grosse et al. 2012]. For the landforms such as scoria cones, pumice cones and obsidian coulees, parameters such as area, width, major axis, minor axis, height, volume, average flank slope, azimuth of major axis, ellipticity, and average irregularity index were analysed. For each landform, these parameters were calculated separately for the edifice, summit and crater, as described in Table 1. In some cases the craters are open to one side; for these volcanic features the morphometric parameters were calculated by considering an estimated closed crater following the method of Grosse et al. [2020]. For rhyolite lava domes and obsidian coulees, all parameters were taken into account for final interpretation, except azimuth of the basal major axis that would be distorted by the flow behaviour of the dome. For the lava flows, only area, width, major axis, and volume were calculated, whereas the maars were treated as craters because the latter two volcanic features are similarly characterised by a depression and do not have topography associated with deposition. Field evidence shows that lava flow landforms are sometimes not fully exposed as they are partially buried under more recent deposits. Therefore, the delineation method following slope breaks only considers those products above the exposed base, while it disregards buried products. Consequently, the morphometric parameters for these landforms might be underestimated [Grosse et al. 2012]. Furthermore, volume of volcanic landforms were retrieved for other MER volcanic complexes (i.e. Corbetti, Aluto, Gedemsa, Boset, and Fentale) using the same approach with the `MORVOLC` algorithm. We define elongated edifices and craters as those having an ellipticity of ≥0.8, as per Paulsen and Wilson [2010]. The height and volume were retrieved from the enclosure profile and 3-D basal surface computed from the three fitting methods (i.e. natural, inverse distance weighted, kriging [Grosse et al. 2012]). These size parameters are reported with the mean and standard deviation of the different values obtained with the different basal extrapolation methods (see Supplementary Material ; Section 5 and Section 6). The height/basal width ratio (H/W_B) and summit width/basal width ratio (W_S/W_B) parameters were also calculated.

Spatial analyses of vent distribution were made using `ArcGIS` and `MATLAB`. To evaluate vent density, spatial analysis was performed for the entire BBTM complex using kernel density functions. The vent clustering was analysed for the entire BBTM volcanic system and in detail by defining nine domains in the volcanic complex based on the vent density map (Section 5.3). The domains were defined by connecting the outermost points of the volcanic vents in a given area [Bruno 2004]. The number of domains (nine) is constrained by qualitative visualisation of the clusters on the vent density map and keeping at least one vent within the defined polygon in order to quantitatively compute the clustering. This enabled us to characterise the spatial distribution of the vents by returning an "R-value". The R-value was calculated as R_a/R_e, with R_a the mean nearest neighbour (NN) distance in a population of known point density, and R_e the expected mean neighbour distance within a Poisson distribution population of equivalent density. R_e is defined as $1/\sqrt{(N\rho_o)}$, where the population density (ρ_0) is defined by the number of vents (N) divided by the volcanic field area. The quality of the fit with the Poisson distribution is quantified by a statistical test (c) that is defined by $R_a - R_e/\sqrt{\sigma_e}$, where σ_e is the standard error of the mean NN distance in the expected distribution. The R value indicates whether the distribution follows a Poisson (R = 1), clustered (R<1), or dispersed (R>1) distribution [Bishop 2007].

Vent alignments were determined through two-point azimuth statistical methods of Lutz [1986] and Cebriá et al. [2011] using the `MATLAB` program of Thomson and Lang [2016]. The Lutz [1986] method considers the azimuth of all segments joining to vents within the study area, without constraint on the maximum distance between vents, and gives the regional preferred alignment. This result is however very dependent on the shape of the analysed area. To eliminate this bias, 100 Monte Carlo simulations of random patterns with the same number of points and spatial extent were run to normalise the raw histogram. Local vent alignment azimuths were also determined using the method of Cebriá et al. [2011]. In this method, the azimuth of vent-to-vent segments were only considered for vents that lie relatively close together, below a threshold distance. The threshold distance is the value equal to $(x - 1\sigma)/3$, where x is the mean separation distance and is the standard deviation.

Finally, we evaluated the volcano-tectonic association by matching the orientation results from the structure, morphometric and vent alignment analyses to understand the influence of the major structures on the magma pathways (Section 6.2).

5 Results

5.1 Structure and lineament analyses

The main surface expression of structures in the study region is in the form of normal faults and fissures aligned with the regional tectonic trends. The fault structures are predominantly

Table 1: Morphometric parameters calculated in this study using the MORVOLC algorithm after Grosse et al. [2012]. When applied to basal edifice (B) or summit (S) for a given landform, the morphometric parameter is indicated with the relevant subscript (e.g. W_B = basal width; W_S = summit width).

Parameter	Unit	Description
Area	km^2	Planimetric area of the (landform, summit, crater) outline
Width	km	Average width of the (landform, summit, crater) base calculated as $2 \times (AB/\pi)^{1/2}$
Major axis	m	Length of the maximum (landform base, summit, crater) diameter passing through the centroid
Minor axis	m	Length of the minimum (landform base, summit, crater) diameter passing through the centroid
Height	m	Difference between the summit elevation and the elevation of the 3-D basal surface below the summit
Crater depth	m	Difference between the lowest crater elevation and the elevation of the 3-D crater surface above this point
Volume	km^3	Volume enclosed between the DEM surface of the landform and the 3-D basal surface
Crater volume	km^3	Volume enclosed between the DEM surface bounded by the crater outline and the 3-D crater surface
Ellipticity		Ellipticity index of the (landform, crater) outline, calculated as minor axis/major axis
Average Irregularity Index		Measure of the complexity of the main elevation contours that enclose the (flank, crater) outline
Height/basal width ratio (H/W_B)		Measure of the overall steepness of the edifice
Summit width/basal width ratio (W_S/W_B)		Measure of the relative size of the summit region
Azimuth of major axis	°	Azimuth (between 0° and 180°) of the direction of (landform base, summit, crater) major axis
Flank average slope	°	Mean and median average slope of the landform excluding the summit region
Crater average slope	°	Mean and median average slope of the crater

sub-vertical (70–85°) trending NNE–SSW, NE–SW, or NW–SE (Figures 2–4). Fissures are predominantly trending in a NNE–SSW direction (Figures 2–4).

The NNE–SSW and NE–SW faults are predominantly exposed in the eastern sector of the volcanic complex where the topography drastically changes from 1900 m asl on the rift floor to 2500 m asl on the eastern plateau (Figure 2). The faults are mainly dipping towards the NW and SE, and the surface on the hanging wall usually shows a tilt towards or away from the rift. In coherent geological formations (e.g. lava flows and ignimbrite), the faults are characterised by steep and prominent scarps. In many cases, the faults die out and/or are not visible in incoherent geological formations, especially in the rhyolite pyroclastic units. The tips of the faults terminate as a tail crack or open fissures extending up to hundreds of metres [Korme et al. 1997]. In a few locations the faults terminate by linking to other faults on relay ramps or by branching out to multiple minor faults (Figure 2A).

The NNE–SSW faults belonging to the WFB are exposed on the youngest rock units in the volcanic complex (i.e. rhyolite pyroclastics, obsidian, scoria and lava flows [Tadesse et al. 2023]). The length-weighted fault statistics of the Wonji faults show a dominant trend of N10° E (Figure 5A). The Wonji faults are mainly characterised by fresh escarpments, short strike lengths (20–4000 m) and small vertical offsets (≤70 m; Figure 5B). The border faults are mainly exposed in the south-eastern sector of the volcanic complex, but further North the Wonji faults become dominant [Figure 2A; Corti et al. 2020]. The border faults form a series of graben and horst structures, displacing the older rock units (Late Pleistocene; i.e. ignimbrites and basalts [Tadesse et al. 2023]). The length-weighted rose diagram indicates that the border faults trend predominantly in a N30° E direction (Figure 5A). These faults are characterised by longer fault lengths (2000–20000 m) and larger vertical displacements (10–250 m) compared to the Wonji faults (Figure 5B).

The lava flows in the central part of the BBTM volcanic system are deformed by NW–SE trending cross-rift faults (Figure 2A), forming a half-graben morphology (Figure 4B). In a few locations these NW–SE faults also transect the rhyolite pyroclastics (Figure 4F). In one field location two NW–SE orienting faults dip in opposite directions (east and west), and the fault planes are filled by white and finer clasts (fault gouge) relative to the hosting pyroclastic deposit (Figure 4F). The cross-rift faults in the BBTM volcanic system are trending in N40° W direction and dipping to the SW with a vertical displacement of 10–150 m (Figure 5B). The NW–SE faults are cross-cut by the NE–SW faults in the south-western part of the BBTM volcanic system (Figure 2A, Figure 4B). In other parts of the MER (e.g. South of Aluto volcano), NW and NE

Figure 4: Field photographs of volcano-tectonic structures in the BBTM volcanic system. The geographic North is indicated by a white arrow on each photo. [A] Regional NE–SW trending border fault, showing fault termination. [B] Regional NW–SE trending cross-rift faults cut by NE–SW trending faults (black arrows). [C] Ring faults located in the southern part of the BBTM volcanic system. [D] Open fissure in a pyroclastic deposit located North of Werdi edifice. [E] Eruptive fissure located North of Miesa. [F] Two opposite dipping faults trending NW–SE in pyroclastic deposits.

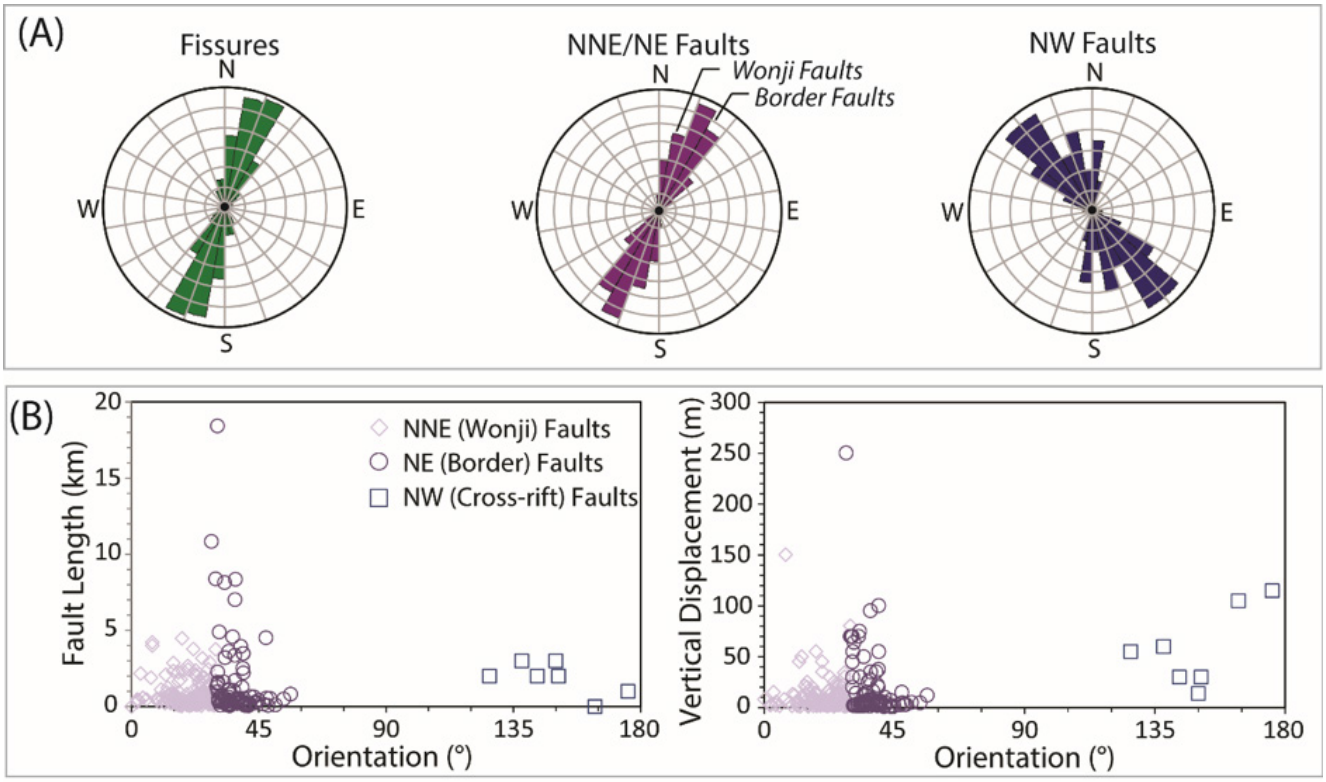

Figure 5: Structural data statistics of the BBTM region. [A] Rose diagram representing frequency of fissures, NNE/NE and NW faults distribution with their respective orientations. The total lengths considered on each rose diagram are 4.2 km (fissure), 248.6 km (NNE/NE fault) and 13 km (NW fault). [B] Bivariate plots of fault length and vertical displacement against fault orientation.

crosscutting faults form rhomboidal structures [Turdu et al. 1999; Corti et al. 2020].

The high-resolution DEM of the BBTM volcanic system shows arcuate faults (i.e. ring faults) exposed in the NE, NW, and SW sectors (near Oda and Bora edifice; Figure 2A) of the complex. Based on field observations and aerial photo and satellite image analysis, Korme [1999] identified segments of ring fault exposed in the NE sector of the BBTM volcanic system, named as "Tullu". The height of the ring faults scarps ranges from 4 to 300 m, with these maximum values observed in the NE. The ring faults are exposed in the ignimbrite and old basalt successions with recent slump cover at the base in the Tullu ring fault, and in the rhyolite pyroclastics elsewhere in the BBTM region (Figure 4C). The ring faults at Tullu are horseshoe-shaped and open to the west, where the faults are sub-vertical and reach the maximum height (i.e. 300 m). The ring faults located in the S and NW parts of the BBTM volcanic system walls are 4–100 m high and show a well-developed drainage network formed by erosion. The Tullu ring fault terminates on the contact with the Wonji faults suggesting the ring fault is older (Figure 2A). The ring faults are also thought to be associated with the collapse or sagging resulting from the identified caldera-forming eruptions [Tadesse et al. 2022].

Fissures are restricted to the eastern sector of the BBTM volcanic system and are aligned with the Wonji and cross-rift faults without any vertical displacement (Figure 2). They occur either as tension fractures (open fissures) or aligned and connected small eruptive centres (eruptive fissures). These features are usually located at the tips of the Wonji faults [Korme et al. 1997]. The length of the fissures reaches up to hundreds of metres. Open fissures have widths of a few cm to 10 m, as confirmed in the field. The open fissure situated immediately north of the Werdi edifice is oriented NW–SE and thus aligns with the cross-rift fault orientation (Figure 4D). In the MER there is abundant evidence of fissures that are associated with soft sediment collapse due to water circulation [e.g. Asfaw 1998], however the open fissures of the BBTM volcanic system described here are attributed to a volcano-tectonic origin, fracturing consolidated rocks (lava and dome) or pyroclastic deposits. The eruptive fissures are associated with young basaltic lava flows with textures varying from highly scoriaceous to massive and porphyritic to aphyric basalt (Figure 4E). Most eruptive fissures are characterised by a ridge-like landform with poor crater preservation. The fissure immediately north of Miesa hosts fresh-looking multiple craters aligned in a NNE–SSW direction. Those craters are well preserved and are ~20–24 m wide, with 5–10 m spacing between the craters.

5.2 Morphometric analyses

5.2.1 *Lava domes*

Eleven silicic domes are mapped in the region (Figure 2A and Figure 3), including the Jima, Togee, and Salen edifices. They are represented on the DEM by positive relief, circular

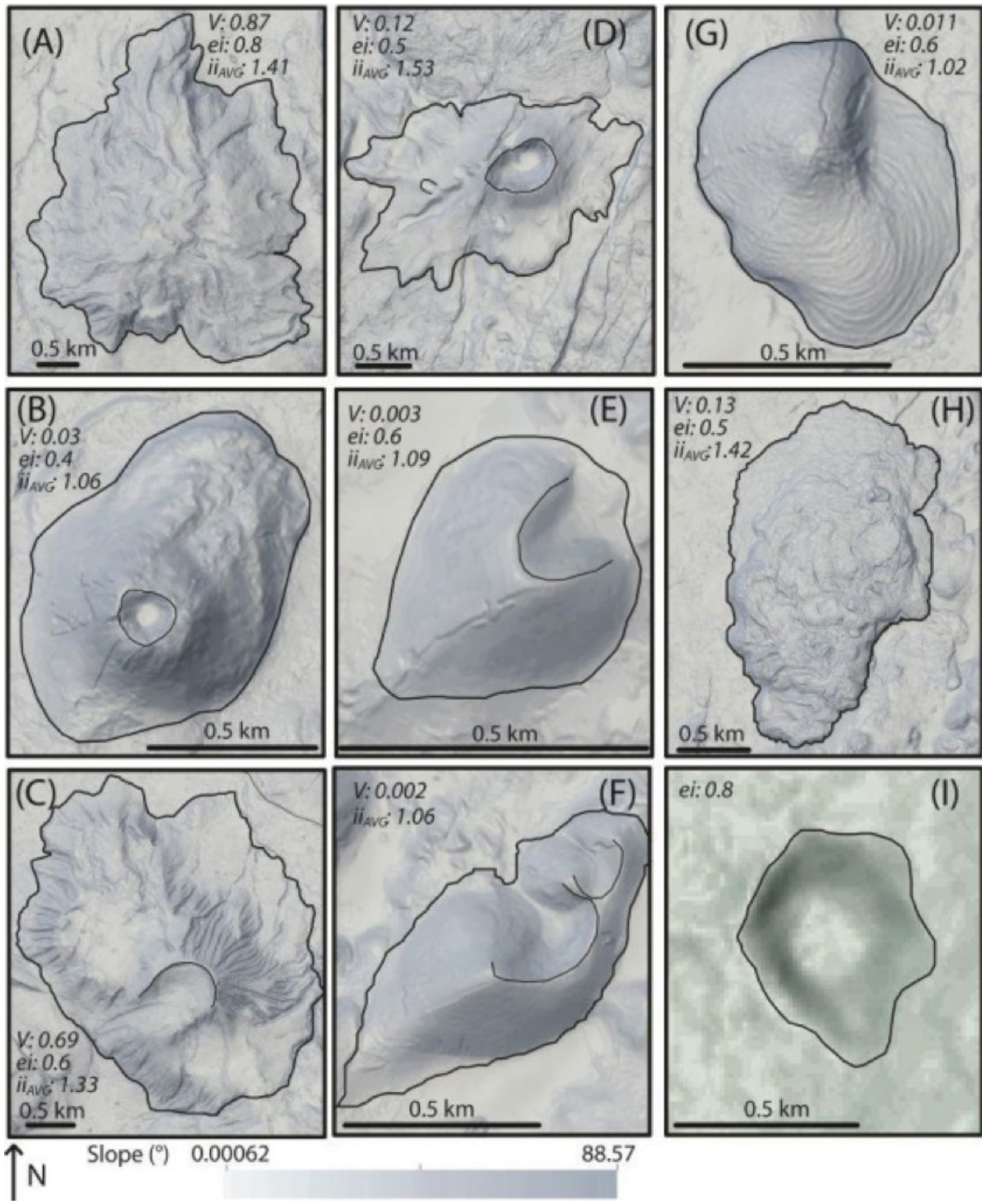

Figure 6: DEM-derived slope maps of some selected volcanic features. [A] Jima and [B] Togee lava domes. [C] Werdi and [D] Tullu Moye pumice cones with open and closed crater, respectively. [E] Horse-shoe scoria cone with open crater. [F] Scoria cone with crater row formed by coalescence of two eruptive centres. [G] and [H] Obsidian coulees with variable surface irregularity and [I] Maar crater. The volume (V, km^3), ellipticity index (ei), average irregularity index (ii_{AVG}) value of each edifice from the morphometric analyses are indicated. The black solid lines indicate the boundary of the edifice and crater (if any). Note that the volcanic features are illustrated using the high resolution LiDAR DEM, but because the LiDAR data have a limited area coverage exceptionally the 12.5 m resolution ALOS PALSAR data is used for the maar.

to sub-circular shape, and in some cases flow morphologies (i.e. flow folds). The lava domes predominantly occur in the central and north-western sectors of the volcanic system (except Salen, which is located in the east) and together they cover a total area of 55 km^2. Most domes are well preserved, however a few of them (Jima and the dome next to Baricha)

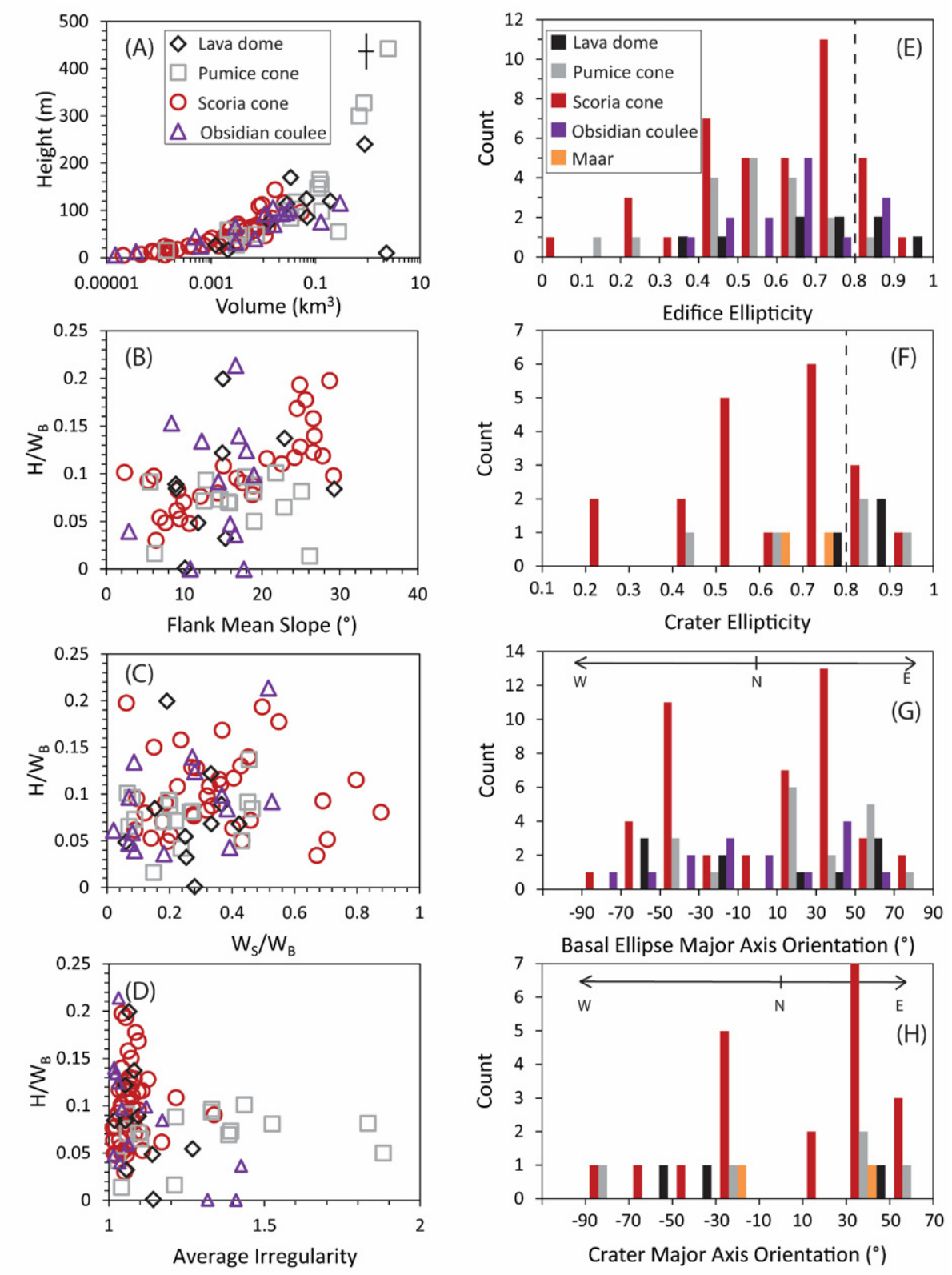

Figure 7: Morphometric parameters binary [A]–[D] and histogram [E]–[H] plots of the analysed scoria cones, pumice cones, lava domes, obsidian coulees, and maars (the latter only included in the histograms). The height/basal width ratio (H/W_B) and summit width/basal width ratio (W_S/W_B) are indicated in abbreviation. The dashed lines on the edifice/crater ellipticity histograms indicate the threshold value (0.8) for considering the geomorphic feature as either elongated ($\leq$0.8) or not, based on Paulsen and Wilson [2010].

show well-developed drainage patterns and evidence of alteration, suggesting a slight degradation (e.g. Figure 6A). Compositionally the domes are silicic, made of aphyric to glassy rhyolites [Tadesse et al. 2023]. The domes have basal widths 0.3–3.5 km, and maximum heights of 240 ± 43 m. The volume varies from 0.001 ± 0.0002 to 0.9 ± 0.2 km^3 (Figure 7). The dome situated next to Baricha has a relatively higher basal width (6.6 km) and volume (2.3 ± 0.3 km^3) than the other lava domes in the BBTM volcanic system, and it also shows features such as flow folds and a gentler slope (10°) indicative of a flow mechanism during its formation. Other domes located in the study region are characterised by steep average flank slopes (average of 15°), and generally high ratios of H/W_B (average of 0.1) and W_S/W_B (average of 0.26), suggesting typical dome morphology [de Silva and Lindsay 2015, ; Figure 7].

Only two domes, Togee and Salen, have a crater on their summit. The craters are generally small (≤315 m width and ~36 m depth) and have a circular shape (i.e. ≥0.8 ellipticity; Figure 6B and Figure 7B). The inner crater walls of the Togee lava dome have a steep mean flank slope (20°) compared to those of the crater of Salen (9°).

5.2.2 *Pumice cones*

Pumice cones are most common in the western sector of the BBTM volcanic system. In total, 18 cones in this category are identified and mapped, including the major edifices such as Baricha, Bora, Oda, Tullu Moye, and Werdi (Figure 3). These are thought to be almost completely composed of silicic (light coloured) pyroclastic deposits based on field evidence (e.g. deep gully cuts on the cone flanks). The pumice cones are represented by a positive relief and circular to elongated shape on the DEM. The pumice cones together cover a total area of 79.5 km^2, without considering the pyroclastic material that blankets the surrounding flat topography, material that may have also originated from the cones. All pumice cones in the study area have a highly irregular flank shape (average of 1.28; Table 2) as a result of dissection by deep gullies and a well-developed drainage pattern, indicating significant degradation (Figure 6C and Figure 8A). The basal width varies from 0.17 to 5.4 km, and cone heights from 15 ± 1 to 442 ± 69 m. The largest pumice edifice (i.e. Bora) volume is 2.5 ± 0.4 km^3. The pumice cones are further characterised by generally low H/W_B (average of 0.07) and W_S/W_B (average of 0.22) (Table 2). The pumice cones have a wide basal ellipticity of 0.2–0.9 (Figure 7). The major axis of the elongated pumice cones (< 0.8 ellipticity; n = 17) shows an orientation of either N10–75° E or N20–44° W.

Some pumice edifices (n = 5) have craters on their summit. Edifices such as Bora, Tullu Moye, and Oda have a well-outlined crater (Figure 6D); on the other hand, edifices such as Werdi have a crater that is open to one side (i.e. breached;Figure 6C). Generally, the craters show significant variation in width (0.4–1.5 km), depth (from 51 ± 2.3 to 251 ± 29 m) and ellipticity (0.6–0.9). The major axis of the elongated craters (i.e. Tullu Moye) is oriented in a N58° E direction. The inner crater slopes are generally gentle (4–16°); especially those of the Oda crater (4°).

5.2.3 *Scoria cones*

Scoria cones are restricted to the eastern part of the BBTM volcanic system and roughly distributed along a NNE–SSW trend (Figure 3). A total of 47 cones in this category are identified and mapped, covering a total area of 11 km^2. Similar to the pumice cones, the scoria cones have a positive relief and circular to elongated shape on the DEM. The cones are predominantly composed of black to brownish pyroclastic deposits (unconsolidated to slightly welded), occasionally with lava flows on their flanks. The scoria cones can be categorised into breached and non-breached cones. There are only few scoria cones with ideal symmetrical cone geometry (Figure 8B). Most are classified as amorphous (non-symmetrical cones), horseshoe-type (one open crater), and crater-raw type (coalescing cones with multiple craters), following terminology proposed by Bemis and Ferencz [2017] (Figure 6 and Figure 8). The scoria cones are generally characterised by an absence of any clear drainage pattern and limited outer flank irregularity (average 1.07; Figure 6E–F). The scoria cones are typically smaller than other landforms in the region, as indicated by their basal width (0.1–1.6 km), height (from 4.4 ± 0.01 to 144 ± 11 m), and volume (maximum 0.05 ± 0.01 km^3) measurements on the DEM (Figure 6A and Figure 6E–F). The scoria cones are generally characterised by higher H/W_B (average of 0.1) and W_S/W_B (average of 0.29) (Table 2). The basal ellipticity of the scoria cones is 0.2–0.9. The major axes of the elliptical scoria cones (n = 43) have a N5–77° E or N25–77° W orientation.

Some scoria cones in the BBTM volcanic system are breached (n = 20), with either isolated or multiple coalesced craters (Figure 6E, F). Overall the craters of the scoria cones are 84–213 m wide and maximum 41 m deep. One crater has a larger size, with a crater width of 350 m. The craters have an ellipticity ranging from 0.5 to 1. The major axes of the elongated craters (n = 18) are oriented N13–61° E or N11–70° W.

5.2.4 *Maars*

Only two maar landforms were found, which are located in the southern part of the volcanic system at a distance of 15 km from Ziway Lake (Figure 1 and Figure 2B). The maars are represented by negative relief on the DEM. Their crater wall is composed of interbedded loose pyroclastic deposit and massive lavas. The pyroclastic layers mainly lapilli-size contain scoria and lithic clasts. The lithics are predominantly green ignimbrite with maximum diameter of 25 cm. The outline of both maar craters is clearly visible and covers a total area of 0.3 km^2, while there is no positive topography around the crater discernible on the DEM (Figure 6I). The maar craters are partially filled by sediments, and have maximum of 0.5 km basal width and 60 m depth. The craters are slightly elongated (~0.7 ellipticity) with their major axis orientation toward N14° W and N31° E. The inner walls of the craters have a slope of >10°.

5.2.5 *Obsidian coulees*

The obsidian coulees are also restricted to the eastern part of the volcanic system (Figure 3). A total of 15 obsidian coulees including Giano, Gnaro, and Miesa are mapped, covering an

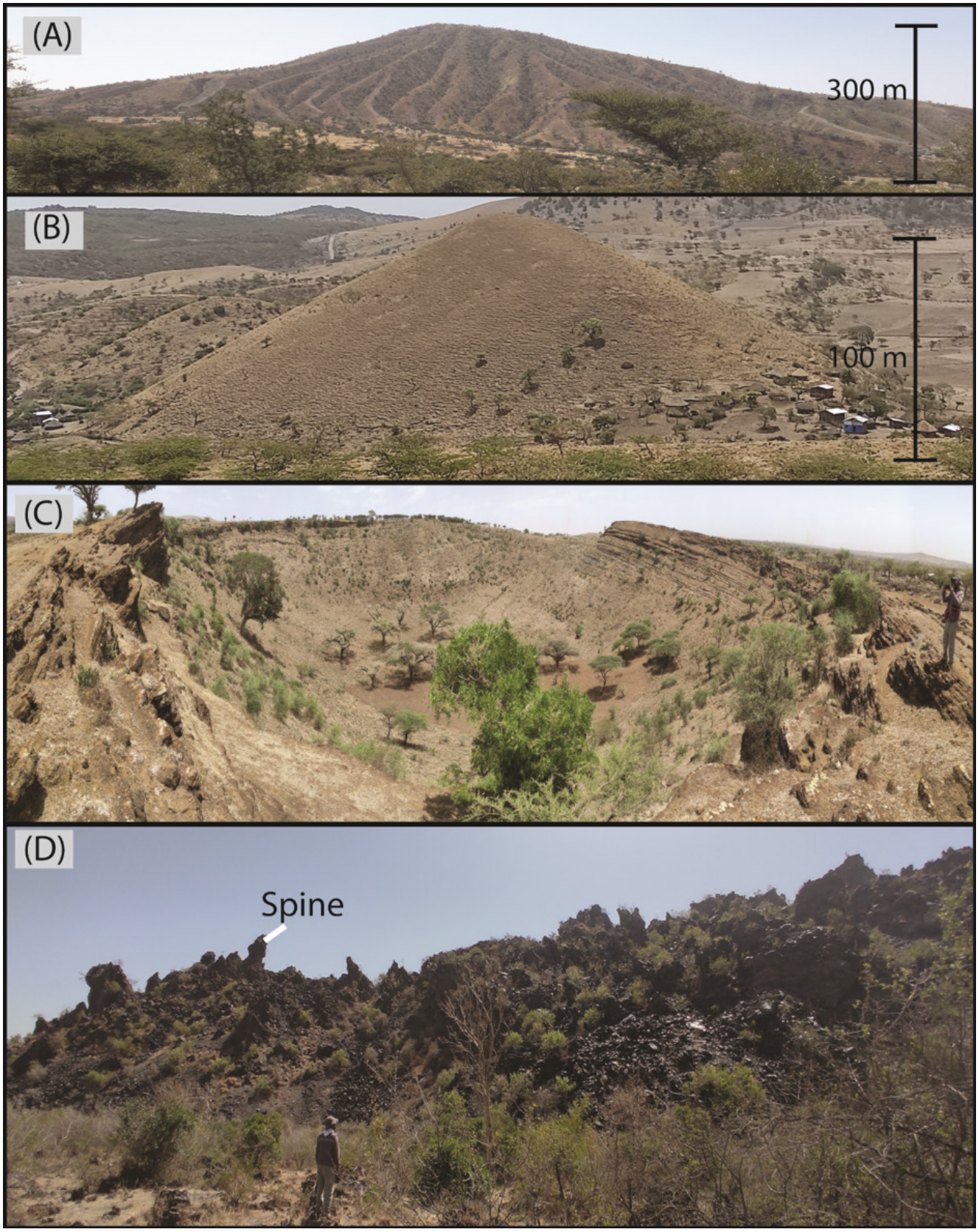

Figure 8: Field photos of selected geomorphologic features. [A] Werdi edifice with a well-developed drainage pattern and deep gullies. [B] Young scoria cone with ideal cone geometry. [C] Maar crater. [D] Giano obsidian coulees with a brecciated surface morphology.

Table 2: Summary of BBTM volcanic features selected morphometric parameters result. Note that all the presented results are average values; the full data set is presented in Supplementary Material 1.

	Lava domes	Pumice cones	Scoria cones	Obsidian coulees
Basal width (km)	1.94	1.91	0.46	0.90
Height (m)	98.15	129.01	44.61	65.18
Volume (km^3)	0.36	0.29	0.01	0.04
Flank mean slope (°)	14.89	17.32	16.05	14.13
Average irregularity index	1.16	1.28	1.07	1.11
Height/basal width (H/W_B)	0.08	0.07	0.10	0.07
Summit width/basal width (W_S/W_B)	0.25	0.22	0.29	0.22

area of 15.2 km^2. They are represented by positive relief, without a crater but with flow structures on the DEM. The obsidian coulees are entirely composed of black obsidian with a crystallinity of ~10%, often with crystal cumulates [Tadesse et al. 2023]. The landforms have well preserved flow banding, wrinkles, and ogives developed during lava emplacement. Additionally, no drainage pattern or deep gullies are observed on the obsidian coulees and they have a regular shape (1.11 average irregularity; e.g. Figure 6G). Obsidian coulees such as Giano are highly brecciated with spines up to 2 m high on the surface (Figure 8D). The size of the obsidian coulees predominantly falls in the range of 0.06 to 1.2 km basal width, from 6 ± 0.8 to 106 ± 22 m height and ≤0.03 km^3 volume (Figure 7A). The Giano and Gnaro obsidian coulees are larger relative to the others in the BBTM volcanic system; they are characterised by 2.1 and 2.7 km basal width, 76 ± 20 and 115 ± 28 m height, and 0.1 ± 0.06 and 0.3 ± 0.05 km^3 volume, respectively. The obsidian coulees have an average flank slope of 14°, 0.07 H/W_B and 0.22 W_S/W_B (Table 2; Figure 7C).

5.2.6 *Lava flows*

Basaltic lava flows predominantly cover the northern and eastern parts of the volcanic complex. In those locations, four different lava flow fields each covering an extensive area (ranging from 0.7 to 19.7 km^2) are identified. Another two localised flow fields (< 4.2 km^2) are found in the centre of the complex (Figure 3). We describe them as lava flow fields because in most places there is no clear exposure, and it is difficult to distinguish individual flow units from one another. In total, an area of ~39 km^2 is covered by the lava flows. Compositionally they are basaltic [Tadesse et al. 2023], moderately vesiculated and typically with an ʻaʻā type morphology. The maximum running distance of the lava flows is 0.4–2.2 km; only one lava flow located at the northern sector of the volcanic system is significantly longer (8.3 km). The total lava flow volume is estimated to be 0.3 km^3, while the individual lava flow field volumes range from 0.002 to 0.2 km^3. The height of the flows is highly variable: the maximum measured thickness in the field is 2.2 m, although the flow base is not exposed.

5.3 Vent spatial analyses

A total of 130 volcanic vents are mapped in the BBTM volcanic system (Figure 9A). These vents are associated with effusive or explosive eruptions with products of either basaltic or rhyolitic composition [Tadesse et al. 2023]. By absolute number, the vents are predominantly concentrated (~60 %, n = 77) in the eastern sector of the volcanic complex, where the vent distribution is extended in the NNE–SSW direction (domain 1, 2, 3, and 4; Figure 9A). Much fewer vents (n = 20) are associated with large edifices such as Bora, and they are mostly parasitic vents on the flank of the main edifice (domain 9; Figure 3). The central, southern and northern sector also have fewer vents (n = 32) (domain 5, 6, 7, and 8; Figure 9A). The Kernel density map and the mean nearest neighbour (NN) distance of the vents in the BBTM volcanic system show vent clustering at a regional level (R = 0.75; Figure 9B, C). As our aim is to investigate the structural controls on the distribution of the volcanic vents, we analysed the vent clustering in the identified nine different domains. The domains located in the east (2, 3, and 4), around Bora (nine) and in the centre (seven), are characterised by a clustered vent distribution (R: 0.52–0.95; Figure 9C). These clustered regions also show a high vent density (maximum of 1.6 vents/km^2; Figure 9) and very small mean NN distance between vents (< 1 km). In contrast, the other domains show a dispersed vent distribution (R: 1.2–2.7) with a lower vent density (0–0.5 vents/km^2) and a higher mean NN distance between the vents (> 4 km; Figure 9C).

Only monogenetic centres are considered for the vent alignment analysis, and so polygenetic centres such as Bora, Baricha, Tullu Moye, Oda, Werdi, and Tullu Moye [Tadesse et al. 2022] are excluded during the analysis. This is in accordance with the criteria commonly used to define monogenetic volcanoes (e.g. ≤ 1 km^3 volume, simple to complex geometry, single eruption episode [Németh 2010; de Silva and Lindsay 2015]). Results of the monogenetic vent alignment analysis using the two-point azimuth method of Lutz [1986] and Cebriá et al. [2011] are shown on Figure 10. The vent alignment at a regional scale is obtained using the Lutz [1986] method, which gives a dominant preferential direction of N65–85° W, N5–35° E and N65–80° E (Figure 10B). The Cebriá et al. [2011] method only considers nearby vents (Section 4) and as a result there is a slight variation with the result from the Lutz [1986] method. The local-scale vent alignment analysis [after Cebriá et al. 2011] gives a high peak in the N0–25° E directions (Figure 10C). The NE vent alignment is focused in the eastern BBTM sector, whereas the NW vent alignment is found predominantly in the central area and near Oda (Figure 10A).

The association of vent location and structural features is very apparent in the eastern sector of the volcanic complex

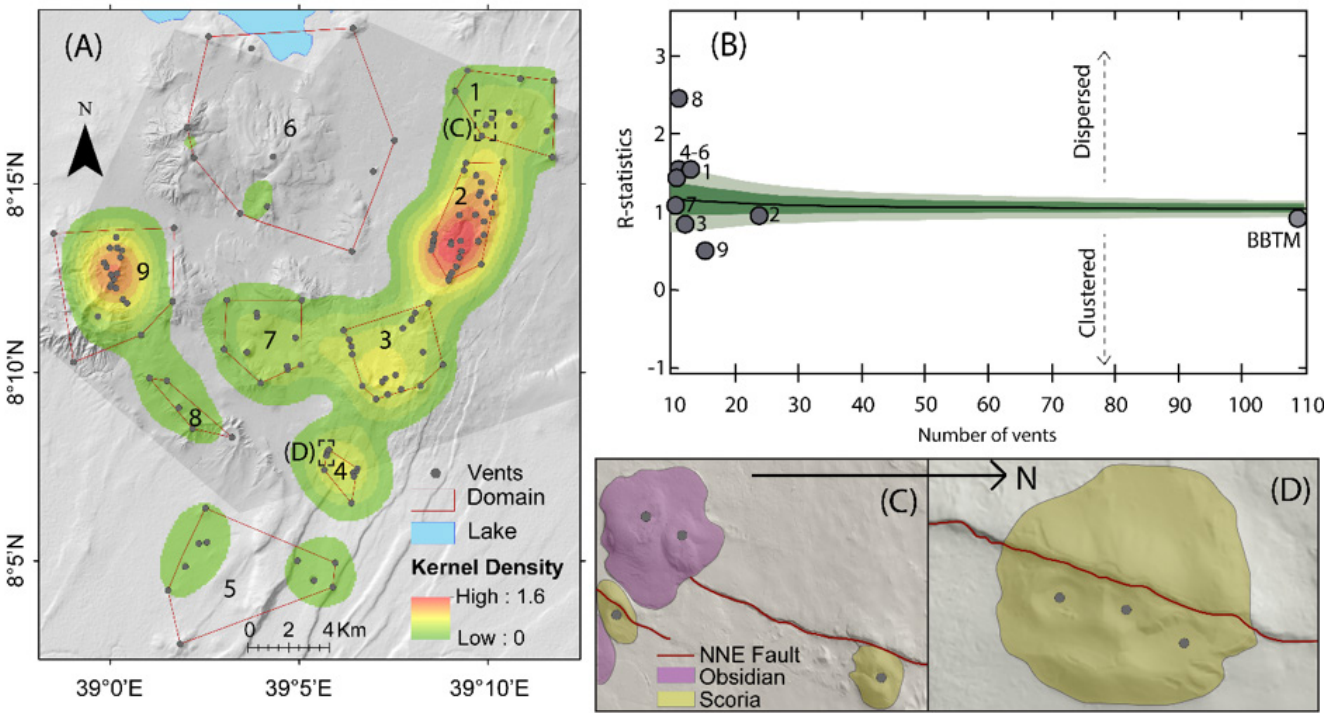

Figure 9: [A] Kernel density map of the vent distribution in the BBTM volcanic system. The vent density is defined as the number of vents per square kilometre area, and a total of nine distinct domains are identified. Dashed rectangles indicate the location of the detailed map of [C] and [D]. [B] Summary of the nearest neighbour (NN) analysis of the domains indicated on figure [A] and overall BBTM volcanic system. The light green coloured shade indicates 2 sigma of the statistical test (Section 4), and the deep green coloured shades are 1 sigma of the statistical test. [C] and [D] Detailed hill-shade map showing an example of spatial connection between volcanic vents and faults. Note that the obsidian coulee is located at the tip of the fault, and the scoria cones are displaced by the faults.

(Figure 3). In this sector, the NNE–SSW fault trend has a strong spatial connection with the vents. In most cases the vents are dissected by the NNE–SSW faults and are situated either at the fault tips or in the middle of the fault on its footwall (Figure 9C and D). In particular, the obsidian coulees (e.g. Miesa) are located at the fault tips (Figure 9C). These obsidian coulees are not dissected by the faults, indicating they are younger or contemporaneous to their connecting fault. On the other hand, the scoria cones are in most cases located at the middle of a fault and they are usually dissected by it (Figure 9D). There is some evidence in the eastern part that a single fault may be associated with both obsidian coulees (occurring at the fault tip) and a scoria cone (around the middle of the fault), despite their widely different eruption behaviour and rock composition (Figure 9C). The areas around Oda and Bora also show a spatial connection between vent locations and the ring faults (Figure 3, Figure 9). Also, in the western part of the volcanic complex, the pumice cones are affected by the fault that connects to them. However, in the central and northern BBTM region, there is no clear field evidence to understand the vent-fault linkage, because these areas are largely covered by lava flows.

6 Discussion

The above-described observations and geostatistical analyses show that the BBTM volcanic system is characterised by different tectonic and volcanic structures, and post-caldera volcanic features. Below we discuss the caldera architecture, volcano-tectonic interaction and magma flux in the BBTM volcanic system and its comparison to other MER complexes, to outline the Late Quaternary volcanic and tectonic interplay in the recent development of the MER.

6.1 BBTM Caldera complex

Calderas are commonly formed by subsidence associated with rapid magma withdrawal from a relatively shallow magmatic reservoir during a large (caldera-forming) eruption [Druitt and Sparks 1984]. A distinctive feature of calderas is the occurrence of inward-facing caldera walls or scarps surrounded by an elevated circular topographic boundary [Branney and Acocella 2015; Acocella 2021]. The significant unloading after caldera formation may drive further magma along a ring-like feeding system during the post-caldera phase of activity, usually leaving traces of eruptive vents aligned along the caldera's walls [Hutchison et al. 2015; Acocella 2021]. Therefore, calderas can be identified by combining investigation on the structural geomorphology (e.g. topographic depression, caldera rim remnants, post-caldera vent distribution) and proximal volcanic products that may have been emplaced during caldera-forming eruptions [Branney and Acocella 2015].

Previous studies suggested that BBTM volcanic system has undergone several caldera-forming events [Korme 1999;

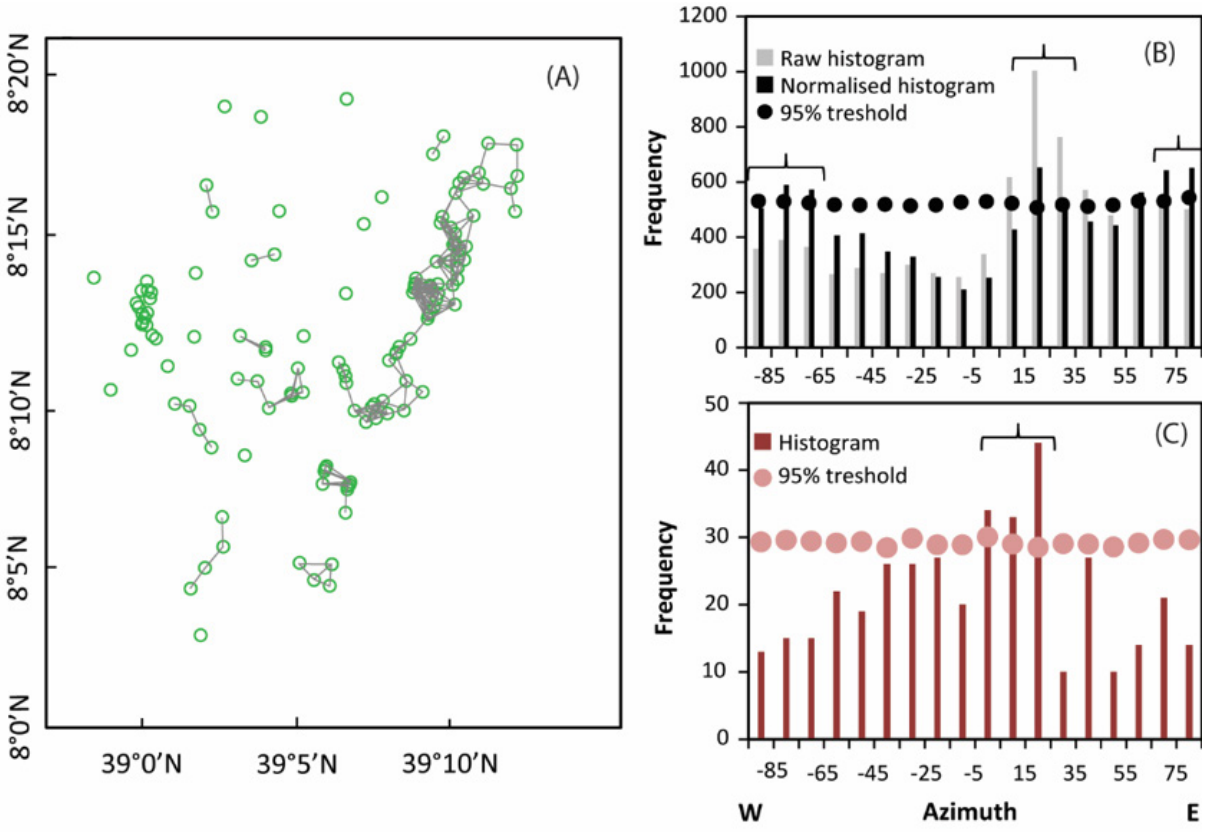

Figure 10: Vent alignment analysis of the monogenetic centres in the BBTM region. [A] Map showing the orientation of the lines connecting pairs of two neighbouring vents. The histograms of the vent alignment orientation are based on the two-point azimuth method of [B] Lutz [1986] and [C] Cebriá et al. [2011]. Raw histogram displays the azimuth between all vents to obtain the regional preferred alignment. Normalised histogram is the azimuth between the vents after 100 Monte Carlo simulations of the raw data to eliminate the bias from analysed area geometry. For each analysis, 100 Monte Carlo models were run and a 95 % threshold value was considered as the critical significant threshold. The dominant preferential direction is indicated by brace brackets.

Tadesse et al. 2022]. Tadesse et al. [2022] investigated the volcanic deposits in the BBTM region and identified deposits from two caldera-forming eruptions (i.e. Suke and Meki). The Suke deposits constitute pumice and lithic lag breccias, whereas the Meki deposits are characterised by very thick successions of tephra fall (>20 m) and pyroclastic density current deposits (>13 m) associated with caldera-forming eruptions [Tadesse et al. 2022]. The age of the older caldera-forming eruption (Suke) is not known because of a lack of datable material [e.g. sanidine; Tadesse et al. 2022]. On the other hand, the last caldera-forming event recorded in the BBTM volcanic system occurred at 107.7 ± 8.8 ka [Tadesse et al. 2022], and which is the youngest one documented in the CMER, but older than Fentale's caldera-forming eruption that is exposed in the NMER (76 ± 18 ka [Vidal et al. 2022]).

The geomorphological study of the BBTM region based on orthophoto, satellite imagery and high-resolution DEM analyses [Korme 1999, this study] helps us to visualise the arcuate (i.e. ring) faults and inward-facing topographic structures that are mainly exposed in the NE, SW and NW part of the BBTM volcanic system, presumably representing caldera rim remnants (Figure 3). Similarly, the vents (predominantly pumice cones) are preferentially aligned with the presumed caldera faults in the SW (near Bora and Oda) and central (Tullu Moye and Werdi) sectors of the BBTM volcanic system (Figure 11). The major challenge in defining the caldera boundaries exists in the SE and W part of the BBTM volcanic system, where the caldera rim remnants are not exposed at the surface. We assume that, in these areas, the structure is eroded and/or covered by post-caldera deposits. Erosion possibly plays a major role in the western part of the BBTM volcanic system, where the rim is completely made of incoherent to poorly welded pyroclastic deposits. Along the eastern part, the region is completely covered by recent volcanic products of lava flows and monogenetic centres which can obscure the caldera structures. These processes (erosion and post-caldera infill) are common in most caldera systems with repeated caldera collapse and caldera-filling volcanism [e.g. Rampey et al. 2010; Hutchison et al. 2015] and mask the caldera rim surface expression [Mahood 1984].

The caldera structure in the BBTM volcanic system is proposed by taking together the evidence from the field investigation of deposits [Tadesse et al. 2022], and observation of caldera rim remnants and eruptive vent alignment (Figure 2A).

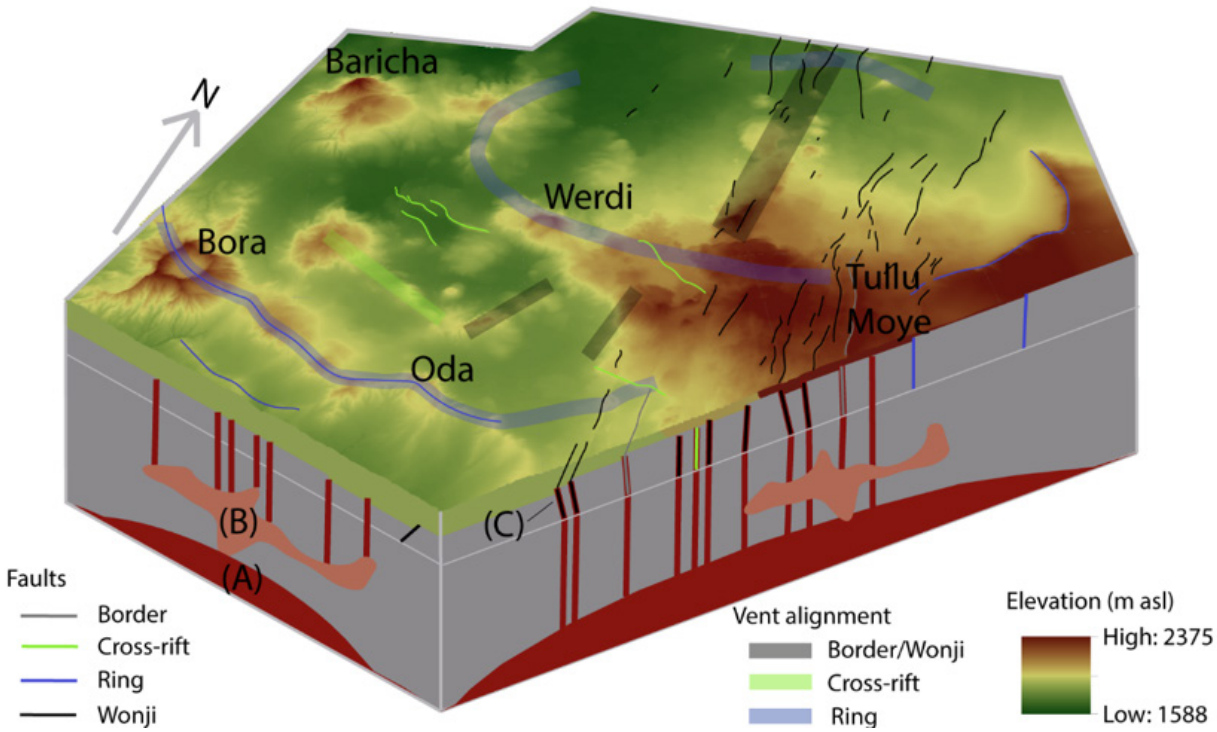

Figure 11: Conceptual model showing the interplay of tectonics and volcanism in the BBTM volcanic complex. The basaltic [A] and rhyolite [B] magmas are stored at different depths and transported through fault network [C]. The ring, cross-rift, Wonji and border faults appear to represent the main pathways for the magma supply in the volcanic system.

We propose two coalescing and sub-circular calderas with a size of 26 × 20 km^2 and 17 × 10 km^2 that explain the observations (Figure 3). Similarly, other volcanoes in the MER such as Kone are characterised by overlap of more than one collapse structure [Rampey et al. 2010]. However, the size of the proposed caldera structure in the BBTM volcanic system is larger than those of the other calderas of the MER peralkaline complexes, which typically have long-axis diameter of ≤ 10 km (i.e. Fentale, Kone, Gedemsa, Aluto and Corbetti [Acocella et al. 2003; Hutchison et al. 2015; Hunt et al. 2019]). Exceptionally, the Shala caldera in the MER has long-axis diameter of 17 km [Mohr et al. 1980], i.e. similar to one of the proposed BBTM calderas. However, the proposed caldera with its long-axis diameter of 26 km from this study is one of the largest ever proposed in the MER. This caldera is more or less similar in dimension to the largest caldera in Japan (i.e. Aso caldera: 25 × 18 km) that has been associated with an eruption of > 600 km^3 dense rock equivalent (DRE) deposited from four consecutive caldera-forming eruption cycles (Aso 1–4 [Bevilacqua et al. 2022, and references therein]). Caldera diameters generally increase with the mass of the associated eruption, therefore, such huge collapse depressions in the BBTM volcanic system are associated with the withdrawal of large volumes of magma that usually signifies extensive volcanic activity for a considerable time period before and during the caldera-forming eruption episode [e.g. Branney and Acocella 2015].

6.2 Volcano-tectonic interaction

Our structural analysis reveals the dissection of the BBTM region by normal faults associated with the regional ~E–W oriented extensional tectonic regime. Due to its geodynamic position, the BBTM volcanic system is a tectonically complex region in the CMER [Korme et al. 1997], which is characterised by a reorientation of the extension direction from E–W (in the rift axis) to NW–SE (in the rift margin) within a distance of a few kilometres [Agostini et al. 2011]. The Wonji and border faults are predominantly exposed on the eastern side of the BBTM volcanic system, where the volcanic centres occur along the en-echelon WFB and where they are located close to the eastern rift margin (Figure 2). The central BBTM region is also affected by few half-graben-forming cross-rift faults (Figure 2), forming rhomboidal structure with the border faults [e.g. Boccaletti et al. 1998; Turdu et al. 1999; Corti 2009; Benvenuti et al. 2023, Figure 2 and Figure 3]. The interaction between the fault systems suggests that the border faults are younger than the cross-rift structures. There is no strong evidence regarding the age relationship between the Wonji and border faults in the BBTM region. However, previous regional studies suggest that the Wonji faults are younger than the border faults, and have been active since ~2 Ma [e.g. WoldeGabriel et al. 1990; Boccaletti et al. 1998; Ebinger and Casey 2001; Bonini et al. 2005; Abebe et al. 2010] and displaces the <10 ka BP lacustrine deposits in the south of the BBTM vol-

canic system (i.e. Langano area [Benvenuti et al. 2013]). The MER border faults at the eastern margin (immediately east of the BBTM volcanic system) reveal active seismicity [e.g. Keir et al. 2006; Lapins et al. 2020], a fresh morphometric expression [Molin and Corti 2015] and Late Pleistocene-Holocene faulting (< 38 ka BP [Agostini et al. 2011; Corti et al. 2020]), which makes it one of the most active margins in the MER.

The surface expression of volcanism often exhibits features associated with past crustal and local stresses during the formation of volcanic features [e.g. Rooney et al. 2011; Corti et al. 2013]. This includes the elongation of edifices and craters, and the alignment of vents that are mainly guided by the orientation of feeder dykes [e.g. Corti et al. 2013; Le Corvec et al. 2013b]. The distribution of volcanic vents may relate to topographic loads and pre-existing or currently active structures that are configured by far- or near-field stresses [e.g. Le Corvec et al. 2013b]. In the BBTM volcanic system only few small volcanic vents are identified as parasitic vents at the base of big edifices (e.g. Bora), suggesting their topographic loads may play a role in deflecting propagating dykes [e.g. Kervyn et al. 2009; Maccaferri et al. 2015]. In most cases the scoria cones, pumice cones, obsidian coulees, lava domes and maars in the BBTM volcanic system stand on relatively flat topography (< 9°), suggesting a limited topographic control on feeding dyke migration [Tibaldi 1995].

Monogenetic edifices are directly linked to magma-filled cracks, or feeder dykes whose orientations record stress field orientation during the time of magma extrusion [Le Corvec et al. 2013a]. Our vent alignment analysis indicates a close relationship between the orientation of the monogenetic vents (e.g. edifice and crater major axis and vent alignment) and the tectonic structures (Figure 10 and Figure 11). The vents show preferential alignment along the Wonji faults (36 %), and significantly along the border (22 %) and cross-rift faults (17 %). The orientation of the elongated craters also confirms a preferential elongation along the same direction (48 % Wonji faults, 22 % border faults, 19 % cross-rift faults). However, the major axis orientation of the elongated edifices reveals a slight difference in the proportion of the vents following the border (36 %) compared to the Wonji faults (30 %), whereas there is no significant proportional change of the vents aligned with the direction of the cross-rift structures (17 %). Deviation of the edifice major axis orientation from the crater major axis and vent alignment may be attributed to varying process distorting the original morphology of the edifice (e.g. partial burial and erosion [Kereszturi and Németh 2012]). Additionally, the ring faults associated with caldera collapse in the BBTM volcanic system (central, south, and SW) play a role in dictating the pathways for magma, as we can understand from the preferential alignment of the pumice cones along an arcuate pattern (Figure 2A and Figure 10). Overall, the magmatic pathways in the BBTM region are mainly controlled by the Wonji faults and by the border, ring and cross-rift faults. This is however not the case for the other MER volcanoes, where the magma pathway (predominantly) follows either the cross-rift (Corbetti, Gedemsa, Fentale [Hunt et al. 2019]), ring (Aluto [Hutchison et al. 2015]) or Wonji faults (Boset [Hunt et al. 2019]). This indicates a complex interaction between tectonics and magma pathways along the MER, resulting from the variable role of regional (i.e. E–W extension) and local stress fields (e.g. pre-existing structures, caldera structures, and edifice load) along the rift.

There is an apparent variation in location, size, and degradation of geomorphic features between the different associated controlling structures. The Wonji and border faults play a great role on the magma pathway of edifices localised in the eastern sector of the BBTM volcanic system (Figure 10). These edifices are mainly scoria cones and obsidian coulees that have a relatively small edifice size (e.g. < 0.1 km^3; Figure 7A; Table 2) and a relatively fresh morphologic appearance (e.g. dominantly > 0.12–0.15 H/W_B, ~1 average irregularity, little weathering and incision; Figure 7B–D). Geochemical data presented by Tadesse et al. [2023] on these edifices suggest that they are composed of basaltic to rhyolitic material (47–74 wt.% SiO_2), and were emplaced by effusive to minor explosive eruptions [Tadesse et al. 2022]. Apart from the BBTM volcanic system, there are very few places in the MER (e.g. Soddo region, SMER [Corti et al. 2013]) where basaltic and rhyolitic magmas extrude from the same tectonic structures.

The ring and cross-rift faults have a dominant role in controlling magma pathways in the western and central parts of the BBTM volcanic system (Figure 10 and Figure 11). The geomorphic features associated with the ring faults are pumice cones with a large edifice size (maximum of 0.8 km^3; Figure 7A) and degraded morphologic appearance (e.g. maximum of 0.1 H/W_B; Figure 7B). The pumice cones are composed of highly evolved rhyolites (70–78 wt.% SiO_2 [Tadesse et al. 2023]) that were emplaced by explosive eruptions [Tadesse et al. 2022]. The vent alignment and elliptical cone/crater major axis orientation proves that the cross-rift faults play an active role in the emplacement of the lava domes and pyroclastic cones in the centre of BBTM volcanic system (Figure 10 and Figure 11). These geomorphic features are characterised by variable size (0.0002–0.2 km^3; Figure 7A), morphologic appearance (e.g. 0.0003–0.2 H/W_B; Fig. Figure 7B), composition (47–78 wt.% SiO_2 [Tadesse et al. 2023]) and eruption behaviour (effusive to explosive [Tadesse et al. 2022]). Overall, the Wonji and border faults (focused in the eastern BBTM volcanic system) promote recent, small and effusive to mildly explosive eruptions of poorly evolved (i.e. basalt) to evolved magma (i.e. comendite) sourced from a depth of 4–29 km [Tadesse et al. 2023], whereas the ring and cross-rift faults act as pathways for explosive eruptions of highly evolved (pantelleritic) magmas sourced from shallow depth (~4 km [Tadesse et al. 2023]) in the western and central sectors of the BBTM volcanic system (Figure 11).

6.3 Along-rift magma flux and implications to the MER evolution

Post-caldera volcanism at BBTM volcanic system includes the formation of domes, cones and lava flows. Since the last caldera collapse (107.7 ka [Tadesse et al. 2022]) a total volume of volcanic products of 9.5 ± 0.4 km^3 was extruded in the BBTM volcanic system. This volume does not consider the explosive volcanic products transported further away by buoyant eruption columns. Tadesse et al. [2022] estimated a

minimum total post-caldera tephra fall volume of 1.4 km^3 for such widespread products. A combined minimum volume of ca. 10.9 km^3 was thus erupted during tens of different eruptions that took place across the BBTM volcanic system since ca. 108 ka. Most products of these eruptions are silicic-explosive (52 %) and silicic-effusive (41.4 %) with subordinate basaltic-explosive (3.1 %) and basaltic-effusive (3.5 %) products. This suggests that the erupted magma composition of the BBTM volcanic system post-caldera phase is predominantly silicic (trachyte–rhyolite), with very few basalts. Using the laboratory-measured bulk density of pyroclastic deposits (basalt: 860 kg m^{-3} and rhyolite: 465 kg m^{-3}; this study) and the melt density reported in the literature (basalt: 2800 kg m^{-3} and rhyolite: 2300 kg m^{-3} [Fierstein and Hildreth 1992; Cruden et al. 1995]), we converted the bulk volume of the explosive volcanic products to the DRE volume, whereas the bulk volume of the effusive volcanic products is assumed to be equal to their DRE volume. This recalculation gives a total DRE volume of 5.6 km^3. The combination of the DRE volume and the youngest caldera age gives a time-averaged magma flux of ca. 0.05 ± 0.02 km^3 ky^{-1} in the last ca. 100 ky.

Recent studies estimated the post-caldera volume of most volcanic complexes situated along the axial zone of the MER [Hutchison et al. 2016; Siegburg et al. 2018; Hunt et al. 2019]. These volume estimations do not consider the tephra falls deposited further away from the volcanoes; therefore the values are underestimated. To better compare with BBTM volcanic system, we recalculated the erupted volumes for each volcanic complex with the `MORVOLC` algorithm [Grosse et al. 2012]. Our volume estimates have a < 1 km^3 difference with the previous studies, except for Boset volcanic complex. For the Boset volcanic complex, the volume estimated by Siegburg et al. [2018] falls within our estimation range which is affected by a large uncertainty (Table 3). Published ages for each caldera [Hutchison et al. 2016; Siegburg et al. 2018; Tadesse et al. 2022; Vidal et al. 2022] are also presented in Table 3. Siegburg et al. [2018] suggest the Boset caldera collapse may have occurred during or after the emplacement of a ~120 ka silicic lava flow and correlate it to the time window of 320–170 ka for CMER caldera-forming eruptions proposed by Hutchison et al. [2016]. There is, however, a wide uncertainty on the Boset caldera age (<119.8 ± 6.1 ka [Siegburg et al. 2018]) and it would require a detailed investigation of the deposits related to the eruption. Relative to BBTM, Boset (0.4 km^3 ky^{-1}) and Corbetti (0.05 km^3 ky^{-1}) have a higher or similar magma flux, whereas Aluto (0.02 km^3 ky^{-1}), Gedemsa (0.001 km^3 ky^{-1}), and Fentale (0.002 km^3 ky^{-1}) seem to be characterised by a lower eruptive flux. The Corbetti and Aluto magma flux is consistent with the ≥ 0.01–0.1 km^3 ky^{-1} estimate by Fontijn et al. [2018] based on post-caldera tephra sequences.

The eruptive flux comparison along the MER generally shows higher values for volcanoes located in the CMER (e.g. Corbetti, Aluto, and BBTM) than those in the NMER (e.g. Fentale). Exceptionally the Boset and Gedemsa volcanoes have extreme high and low eruptive flux estimates, respectively, that may require further scrutiny in future studies. The responsible factors for the along-rift variation in volcanism may be associated with heterogeneity of magma generation, storage and transport in the mantle and lithosphere, respectively [Keir et al. 2015; Iddon et al. 2019]. Geophysical studies (i.e. seismic anisotropy, shear wave splitting, and regional mantle tomography) confirm the presence of relatively high melt volumes beneath the CMER compared with the SMER and NMER [Bastow et al. 2008; Hammond et al. 2014]. The CMER also has a younger rifting history than elsewhere in the MER [WoldeGabriel et al. 1990; Bonini et al. 2005; Abebe et al. 2010]: younger plate stretching could contribute to increased magma generation since the thermal anomaly created by asthenospheric upwelling is more prominent than in the surrounding areas [Bastow et al. 2008; Keir et al. 2015].

The mantle-derived magmas are transported to the upper lithosphere and mostly stored for a while before eruption [e.g. Iddon et al. 2019; Tadesse et al. 2023]. Magma storage conditions (e.g. temperature, pressure, volatile content) at shallow level have a great impact on the magma eruptibility [e.g. Annen et al. 2008; Gelman et al. 2013]. Previous work suggests some difference in shallow level storage conditions of the (silicic) magmas at Aluto (718–765 °C, 5.4 km [Gleeson et al. 2017]) and the BBTM (700–900 °C, 4 km [Tadesse et al. 2023]). The higher magma temperature in the BBTM volcanic system relative to those in Aluto volcano may explain the contrast in the eruptive flux between the two volcanoes in combination with the faulting (as discussed in Section 6.2). There is no comparative information for the other volcanoes (Corbetti and Fentale) to identify any systematic contrast or gradient along the MER. Moreover, the interplay of faulting and gravitational unloading associated with far-field tectonic forces and crustal thinning also plays a great role on the magma supply within the lithosphere [Maccaferri et al. 2015; Chambers et al. 2021]. As a consequence, the dominance of WFB and the thinner crust in the CMER and NMER relative to the SMER may facilitate magma eruption in those first two sectors of the MER relative to the latter [Mackenzie et al. 2005; Maguire et al. 2006; Keranen et al. 2009; Agostini et al. 2011].

7 Conclusion

Morphometric, structural, and vent spatial analyses provide new insights into the relationship of tectonics and volcanism in the MER. The structural analysis of the BBTM volcanic system reveals evidence of various tectonic structures in the complex. The NNE–SSW (Wonji faults), NE–SW (border faults), and NW–SE (cross-rift faults) faults are the major tectonic structures and each have different fault orientation, fault length, vertical displacement and fault density. The temporal relationships in the field suggest that the border faults are younger than the cross-rift faults. The observed caldera rim remnants on the high-resolution DEM are explained by at least two coalescing elliptical calderas with a size of 26 × 20 km^2 and 17 × 10 km^2. The common BBTM volcanic system post-caldera landforms are lava domes, pumice cones, scoria cones, maars, obsidian coulees, and lava flows, which have distinct morphological characteristics. Vent elongation and alignment analysis suggests that the post-caldera landforms are highly associated with the caldera(s) and tectonic structures, highlighting that these structures have acted as magma pathways during the recent eruptions at the BBTM volcanic

Table 3: Post-caldera erupted volume and post-caldera magma flux estimate for selected MER volcanic complexes. Caldera ages and post-caldera eruptive volume estimates from previous studies are presented. The volume of post-caldera volcanic products at Boset volcano (Boset-Bericha Volcanic Complex) is calculated based on the estimate of Siegburg et al. [2018] subtracting the pre-caldera phases (A0, A1, A2, B; ~11 km^3) from the total Boset-Bericha Volcanic Complex (~65 km^3) volume.

Volcano	Caldera age (ka)			Volume (km^3)				DRE (km^3)	Magma flux (km^3 ky^{-1})		
				Literature	This study						
Fentale	76	±	18*	<1§	0.1	±	0.03	0.1	0.002	±	0.0004
Boset	< 119.8	±	6.1**	~54**	48.3	±	8.5	48.2	0.4	±	0.07
Gedemsa	251	±	47*	1‡, <1§	0.4	±	0.05	0.3	0.001	±	0.0004
BBTM	107.7	±	8.8†		10.9	±	0.4	5.6	0.05	±	0.02
Aluto	306 ± 12	–	316 ± 19‡	27‡	26.6	±	0.8	6.7	0.02	±	0.01
Corbetti	182	±	28‡	15‡, 14.5§	14.3	±	0.9	8.7	0.05	±	0.02

* Vidal et al. [2022]
** Siegburg et al. [2018]
† Tadesse et al. [2022]
‡ Hutchison et al. [2016]
§ Hunt et al. [2019]

system. The Wonji and border faults (focused in the eastern BBTM volcanic system) promote recent, small and effusive to mildly explosive eruptions of basaltic and comenditic magma sources from a great depth (4–29 km), while the ring and cross-rift faults act as pathways for explosive eruptions of highly evolved pantelleritic magmas sourced from shallow depth (~4 km) in the western and central sectors of the BBTM volcanic system. During the BBTM post-caldera phase, a total volume of 10.9 km^3 (i.e. DRE = 5.6 km^3) of mostly silicic magma was erupted, at an average rate of 0.05 km^3 ky^{-1}.

Author Contributions

AT was responsible for conceptualising the project, leading the field work, compiling data, analysing and interpreting results, and writing and making figures. GB assisted in the field work and manuscript editing. MK, AM, SG, GY and DA contributed to conceptualising the project and manuscript editing. KF contributed by supervising and conceptualising the project and editing the manuscript.

Acknowledgements

AT is supported by a Fonds National de la Recherche Scientifique (F.R.S.-FNRS) Aspirant doctoral fund. The high-resolution LiDAR data of the study region is kindly provided by Tulu Moye Geothermal Operations PLC (TMGO). Field work in Ethiopia was permitted by authorities of the Oromia regional state, and professional logistical support was provided by Ethioder Pvt Ltd Co. We thank Daniel O'Hara for sharing the MATLAB source code and fruitful discussion on the MORVOLC algorithm. KF acknowledges support from the Wiener-Anspach Foundation and FNRS MIS grant F.4515.20F. Our gratitude goes to Michael James and Jamie I. Farquharson for editorial handling, and two anonymous reviewers for detailed and constructive comments which improved the paper.

Data Availability

All data utilized in this work are comprehensively presented, and the morphometric data are summarized within the Supplementary Material found online alongside this article.

Copyright Notice

References

Abebe, B., V. Acocella, T. Korme, and D. Ayalew (2007). "Quaternary faulting and volcanism in the Main Ethiopian Rift". *Journal of African Earth Sciences* 48(2–3), pages 115–124. DOI: 10.1016/j.jafrearsci.2006.10.005.

Abebe, B., M. Boccaletti, R. Mazzuoli, M. Bonini, L. Tortorici, and T. Trua (1998). *Geological map of the Lake Ziway – Asella region (Main Ethiopian Rift)*. [Scale 1:50,000].

Abebe, T., M. L. Balestrieri, and G. Bigazzi (2010). "The Central Main Ethiopian Rift is younger than 8Ma: confirmation through apatite fission-track thermochronology". *Terra Nova* 22(6), pages 470–476. DOI: 10.1111/j.1365-3121.2010.00968.x.

Abebe Adhana, T. (2014). "The occurrence of a complete continental rift type of volcanic rocks suite along the Yerer–Tullu Wellel Volcano Tectonic Lineament, Central Ethiopia". *Journal of African Earth Sciences* 99, pages 374–385. DOI: 10.1016/j.jafrearsci.2014.02.008.

Acocella, V., T. Korme, F. Salvini, and R. Funiciello (2003). "Elliptic calderas in the Ethiopian Rift: control of pre-existing structures". *Journal of Volcanology and Geothermal Re-*

search 119(1-4), pages 189–203. DOI: 10.1016/s0377-0273(02)00342-6.

Acocella, V. (2021). *Volcano-Tectonic Processes*. Springer International Publishing. ISBN: 978-3-030-65968-4. DOI: 10.1007/978-3-030-65968-4.

Agostini, A., M. Bonini, G. Corti, F. Sani, and F. Mazzarini (2011). "Fault architecture in the Main Ethiopian Rift and comparison with experimental models: Implications for rift evolution and Nubia–Somalia kinematics". *Earth and Planetary Science Letters* 301(3–4), pages 479–492. DOI: 10.1016/j.epsl.2010.11.024.

Albino, F. and J. Biggs (2021). "Magmatic Processes in the East African Rift System: Insights From a 2015–2020 Sentinel-1 InSAR Survey". *Geochemistry, Geophysics, Geosystems* 22(3). DOI: 10.1029/2020gc009488.

Annen, C., M. Pichavant, O. Bachmann, and A. Burgisser (2008). "Conditions for the growth of a long-lived shallow crustal magma chamber below Mount Pelee volcano (Martinique, Lesser Antilles Arc)". *Journal of Geophysical Research* 113(B7). DOI: 10.1029/2007jb005049.

Asfaw, L. M. (1998). "Environmental hazard from fissures in the Main Ethiopian Rift". *Journal of African Earth Sciences* 27(3-4), pages 481–490. DOI: 10.1016/s0899-5362(98)00074-8.

Bastow, I. D., A. A. Nyblade, G. W. Stuart, T. O. Rooney, and M. H. Benoit (2008). "Upper mantle seismic structure beneath the Ethiopian hot spot: Rifting at the edge of the African low-velocity anomaly". *Geochemistry, Geophysics, Geosystems* 9(12). DOI: 10.1029/2008gc002107.

Bemis, K. G. and M. Ferencz (2017). "Morphometric analysis of scoria cones: the potential for inferring process from shape". *Geological Society, London, Special Publications* 446(1), pages 61–100. DOI: 10.1144/sp446.9.

Benvenuti, M., M. Bonini, F. Tassi, G. Corti, F. Sani, A. Agostini, P. Manetti, and O. Vaselli (2013). "Holocene lacustrine fluctuations and deep CO2 degassing in the northeastern Lake Langano Basin (Main Ethiopian Rift)". *Journal of African Earth Sciences* 77, pages 1–10. DOI: 10.1016/j.jafrearsci.2012.09.001.

Benvenuti, M., G. Corti, D. Keir, and F. Sani (2023). "Transverse tectonics control on the Late Quaternary development of the Central Main Ethiopian Rift". *Italian Journal of Geosciences* 142(1), pages 42–56. DOI: 10.3301/ijg.2023.05.

Bevilacqua, A., A. Aravena, W. Aspinall, A. Costa, S. Mahony, A. Neri, S. Sparks, and B. Hill (2022). "Assessing minimum pyroclastic density current mass to impact critical infrastructures: example from Aso caldera (Japan)". *Natural Hazards and Earth System Sciences* 22(10), pages 3329–3348. DOI: 10.5194/nhess-22-3329-2022.

Biggs, J., I. D. Bastow, D. Keir, and E. Lewi (2011). "Pulses of deformation reveal frequently recurring shallow magmatic activity beneath the Main Ethiopian Rift". *Geochemistry, Geophysics, Geosystems* 12(9), n/a–n/a. DOI: 10.1029/2011gc003662.

Bishop, M. A. (2007). "Point pattern analysis of eruption points for the Mount Gambier volcanic sub-province: a quantitative geographical approach to the understanding of volcano distribution". *Area* 39(2), pages 230–241. DOI: 10.1111/j.1475-4762.2007.00729.x.

Boccaletti, M., M. Bonini, R. Mazzuoli, B. Abebe, L. Piccardi, and L. Tortorici (1998). "Quaternary oblique extensional tectonics in the Ethiopian Rift (Horn of Africa)". *Tectonophysics* 287(1-4), pages 97–116. DOI: 10.1016/s0040-1951(98)80063-2.

Bonini, M., G. Corti, F. Innocenti, P. Manetti, F. Mazzarini, T. Abebe, and Z. Pecskay (2005). "Evolution of the Main Ethiopian Rift in the frame of Afar and Kenya rifts propagation". *Tectonics* 24(1), n/a–n/a. DOI: 10.1029/2004tc001680.

Branney, M. and V. Acocella (2015). "Calderas". *The Encyclopedia of Volcanoes*. Edited by H. Sigurdsson, B. Houghton, S. R. McNutt, H. Rymer, and J. Stix. 2nd edition. Elsevier, pages 299–315. DOI: 10.1016/b978-0-12-385938-9.00016-x.

Bruno, B. C. (2004). "Clustering within rootless cone groups on Iceland and Mars: Effect of nonrandom processes". *Journal of Geophysical Research* 109(E7). DOI: 10.1029/2004je002273.

Casey, M., C. Ebinger, D. Keir, R. Gloaguen, and F. Mohamed (2006). "Strain accommodation in transitional rifts: extension by magma intrusion and faulting in Ethiopian rift magmatic segments". *Geological Society, London, Special Publications* 259(1), pages 143–163. DOI: 10.1144/gsl.sp.2006.259.01.13.

Cebriá, J., C. Martín-Escorza, J. López-Ruiz, D. Morán-Zenteno, and B. Martiny (2011). "Numerical recognition of alignments in monogenetic volcanic areas: Examples from the Michoacán-Guanajuato Volcanic Field in Mexico and Calatrava in Spain". *Journal of Volcanology and Geothermal Research* 201(1–4), pages 73–82. DOI: 10.1016/j.jvolgeores.2010.07.016.

Chambers, E. L., N. Harmon, C. A. Rychert, and D. Keir (2021). "Variations in melt emplacement beneath the northern East African Rift from radial anisotropy". *Earth and Planetary Science Letters* 573, page 117150. DOI: 10.1016/j.epsl.2021.117150.

Corti, G. (2009). "Continental rift evolution: From rift initiation to incipient break-up in the Main Ethiopian Rift, East Africa". *Earth-Science Reviews* 96(1-2), pages 1–53. DOI: 10.1016/j.earscirev.2009.06.005.

Corti, G., D. Maestrelli, and F. Sani (2022). "Large-to Local-Scale Control of Pre-Existing Structures on Continental Rifting: Examples From the Main Ethiopian Rift, East Africa". *Frontiers in Earth Science* 10. DOI: 10.3389/feart.2022.808503.

Corti, G., P. Molin, A. Sembroni, I. D. Bastow, and D. Keir (2018a). "Control of Pre-rift Lithospheric Structure on the Architecture and Evolution of Continental Rifts: Insights From the Main Ethiopian Rift, East Africa". *Tectonics* 37(2), pages 477–496. DOI: 10.1002/2017tc004799.

– (2018b). "Control of Pre-rift Lithospheric Structure on the Architecture and Evolution of Continental Rifts: Insights From the Main Ethiopian Rift, East Africa". *Tectonics* 37(2), pages 477–496. DOI: 10.1002/2017tc004799.

Corti, G., F. Sani, A. A. Florio, T. Greenfield, D. Keir, A. Erbello, A. A. Muluneh, and A. Ayele (2020). "Tectonics of the Asela-Langano Margin, Main Ethiopian Rift (East Africa)". *Tectonics* 39(8). DOI: 10.1029/2020tc006075.

Corti, G., F. Sani, M. Philippon, D. Sokoutis, E. Willingshofer, and P. Molin (2013). "Quaternary volcano-tectonic activity in the Soddo region, western margin of the Southern Main Ethiopian Rift". *Tectonics*, n/a–n/a. DOI: 10.1002/tect.20052.

Cruden, A., H. Koyi, and H. Schmeling (1995). "Diapiric basal entrainment of mafic into felsic magma". *Earth and Planetary Science Letters* 131(3-4), pages 321–340. DOI: 10.1016/0012-821x(95)00033-9.

Daniels, K., I. Bastow, D. Keir, R. Sparks, and T. Menand (2014). "Thermal models of dyke intrusion during development of continent–ocean transition". *Earth and Planetary Science Letters* 385, pages 145–153. DOI: 10.1016/j.epsl.2013.09.018.

de Silva, S. and J. M. Lindsay (2015). "Primary Volcanic Landforms". *The Encyclopedia of Volcanoes*. Edited by H. Sigurdsson, B. Houghton, S. R. McNutt, H. Rymer, and J. Stix. 2nd edition. Elsevier, pages 273–297. DOI: 10.1016/b978-0-12-385938-9.00015-8.

Di Paola, G. M. (1972). "The Ethiopian Rift Valley (between 7° 00′ and 8° 40′ lat. north)". *Bulletin Volcanologique* 36(4), pages 517–560. DOI: 10.1007/bf02599823.

Druitt, T. H. and R. S. J. Sparks (1984). "On the formation of calderas during ignimbrite eruptions". *Nature* 310(5979), pages 679–681. DOI: 10.1038/310679a0.

Ebinger, C. J., T. Yemane, G. WoldeGabriel, J. L. Aronson, and R. C. Walter (1993). "Late Eocene–Recent volcanism and faulting in the southern main Ethiopian rift". *Journal of the Geological Society* 150(1), pages 99–108. DOI: 10.1144/gsjgs.150.1.0099.

Ebinger, C. and M. Casey (2001). "Continental breakup in magmatic provinces: An Ethiopian example". *Geology* 29(6), page 527. DOI: 10.1130/0091-7613(2001)029<0527:cbimpa>2.0.co;2.

Fierstein, J. and W. Hildreth (1992). "The plinian eruptions of 1912 at Novarupta, Katmai National Park, Alaska". *Bulletin of Volcanology* 54(8), pages 646–684. DOI: 10.1007/bf00430778.

Fontijn, K., K. McNamara, A. Zafu Tadesse, D. M. Pyle, F. Dessalegn, W. Hutchison, T. A. Mather, and G. Yirgu (2018). "Contrasting styles of post-caldera volcanism along the Main Ethiopian Rift: Implications for contemporary volcanic hazards". *Journal of Volcanology and Geothermal Research* 356, pages 90–113. DOI: 10.1016/j.jvolgeores.2018.02.001.

Gelman, S. E., F. J. Gutiérrez, and O. Bachmann (2013). "On the longevity of large upper crustal silicic magma reservoirs". *Geology* 41(7), pages 759–762. DOI: 10.1130/g34241.1.

Gleeson, M. L., M. J. Stock, D. M. Pyle, T. A. Mather, W. Hutchison, G. Yirgu, and J. Wade (2017). "Constraining magma storage conditions at a restless volcano in the Main Ethiopian Rift using phase equilibria models". *Journal of Volcanology and Geothermal Research* 337, pages 44–61. DOI: 10.1016/j.jvolgeores.2017.02.026.

Greenfield, T., D. Keir, J.-M. Kendall, and A. Ayele (2019). "Seismicity of the Bora-Tullu Moye Volcanic Field, 2016–2017". *Geochemistry, Geophysics, Geosystems* 20(2), pages 548–570. DOI: 10.1029/2018gc007648.

Grosse, P., M. L. Ochi Ramacciotti, F. Escalante Fochi, S. Guzmán, Y. Orihashi, and H. Sumino (2020). "Geomorphology, morphometry, spatial distribution and ages of mafic monogenetic volcanoes of the Peinado and Incahuasi fields, southernmost Central Volcanic Zone of the Andes". *Journal of Volcanology and Geothermal Research* 401, page 106966. DOI: 10.1016/j.jvolgeores.2020.106966.

Grosse, P., B. van Wyk de Vries, P. A. Euillades, M. Kervyn, and I. A. Petrinovic (2012). "Systematic morphometric characterization of volcanic edifices using digital elevation models". *Geomorphology* 136(1), pages 114–131. DOI: 10.1016/j.geomorph.2011.06.001.

Hammond, J. O. S., J.-M. Kendall, J. Wookey, G. W. Stuart, D. Keir, and A. Ayele (2014). "Differentiating flow, melt, or fossil seismic anisotropy beneath Ethiopia". *Geochemistry, Geophysics, Geosystems* 15(5), pages 1878–1894. DOI: 10.1002/2013gc005185.

Hunt, J. A., T. A. Mather, and D. M. Pyle (2020). "Morphological comparison of distributed volcanic fields in the Main Ethiopian Rift using high-resolution digital elevation models". *Journal of Volcanology and Geothermal Research* 393, page 106732. DOI: 10.1016/j.jvolgeores.2019.106732.

Hunt, J. A., D. M. Pyle, and T. A. Mather (2019). "The Geomorphology, Structure, and Lava Flow Dynamics of Peralkaline Rift Volcanoes From High-Resolution Digital Elevation Models". *Geochemistry, Geophysics, Geosystems* 20(3), pages 1508–1538. DOI: 10.1029/2018gc008085.

Hutchison, W., R. Fusillo, D. M. Pyle, T. A. Mather, J. D. Blundy, J. Biggs, G. Yirgu, B. E. Cohen, R. A. Brooker, D. N. Barfod, and A. T. Calvert (2016). "A pulse of mid-Pleistocene rift volcanism in Ethiopia at the dawn of modern humans". *Nature Communications* 7(1). DOI: 10.1038/ncomms13192.

Hutchison, W., T. A. Mather, D. M. Pyle, J. Biggs, and G. Yirgu (2015). "Structural controls on fluid pathways in an active rift system: A case study of the Aluto volcanic complex". *Geosphere* 11(3), pages 542–562. DOI: 10.1130/ges01119.1.

Iddon, F., C. Jackson, W. Hutchison, K. Fontijn, D. M. Pyle, T. A. Mather, G. Yirgu, and M. Edmonds (2019). "Mixing and Crystal Scavenging in the Main Ethiopian Rift Revealed by Trace Element Systematics in Feldspars and Glasses". *Geochemistry, Geophysics, Geosystems* 20(1), pages 230–259. DOI: 10.1029/2018gc007836.

Jonsson, S. (2016). *Remote Sensing in Tulu Moye. Orthophotos and LiDAR DTM*. Technical report. 19 pages.

Keir, D., I. D. Bastow, G. Corti, F. Mazzarini, and T. O. Rooney (2015). "The origin of along-rift variations in faulting and magmatism in the Ethiopian Rift". *Tectonics* 34(3), pages 464–477. DOI: 10.1002/2014tc003698.

Keir, D., C. J. Ebinger, G. W. Stuart, E. Daly, and A. Ayele (2006). "Strain accommodation by magmatism and faulting as rifting proceeds to breakup: Seismicity of the northern Ethiopian rift". *Journal of Geophysical Research: Solid Earth* 111(B5), n/a–n/a. DOI: 10.1029/2005jb003748.

Keranen, K. and S. Klemperer (2008). "Discontinuous and diachronous evolution of the Main Ethiopian Rift: Implications for development of continental rifts". *Earth and Planetary Science Letters* 265(1–2), pages 96–111. DOI: 10.1016/j.epsl.2007.09.038.

Keranen, K. M., S. L. Klemperer, J. Julia, J. F. Lawrence, and A. A. Nyblade (2009). "Low lower crustal velocity across Ethiopia: Is the Main Ethiopian Rift a narrow rift in a hot craton?" *Geochemistry, Geophysics, Geosystems* 10(5), n/a–n/a. DOI: 10.1029/2008gc002293.

Kereszturi, G. and K. Németh (2012). "Structural and morphometric irregularities of eroded Pliocene scoria cones at the Bakony–Balaton Highland Volcanic Field, Hungary". *Geomorphology* 136(1), pages 45–58. DOI: 10.1016/j.geomorph.2011.08.005.

Kervyn, M., G. G. J. Ernst, B. van Wyk de Vries, L. Mathieu, and P. Jacobs (2009). "Volcano load control on dyke propagation and vent distribution: Insights from analogue modeling". *Journal of Geophysical Research* 114(B3). DOI: 10.1029/2008jb005653.

Kervyn, M., G. Ernst, J.-C. Carracedo, and P. Jacobs (2012). "Geomorphometric variability of "monogenetic" volcanic cones: Evidence from Mauna Kea, Lanzarote and experimental cones". *Geomorphology* 136(1), pages 59–75. DOI: 10.1016/j.geomorph.2011.04.009.

Kogan, L., S. Fisseha, R. Bendick, R. Reilinger, S. McClusky, R. King, and T. Solomon (2012). "Lithospheric strength and strain localization in continental extension from observations of the East African Rift". *Journal of Geophysical Research: Solid Earth* 117(B3). DOI: 10.1029/2011jb008516.

Korme, T. (1999). "Lithologic and structural mapping of the northeast Lake Ziway area, Ethiopian Rift, with the help of landsat tm data." *SINET: Ethiopian Journal of Science* 22(2), pages 151–174.

Korme, T., J. Chorowicz, B. Collet, and F. F. Bonavia (1997). "Volcanic vents rooted on extension fractures and their geodynamic implications in the Ethiopian Rift". *Journal of Volcanology and Geothermal Research* 79(3-4), pages 205–222. DOI: 10.1016/s0377-0273(97)00034-6.

Lapins, S., J. M. Kendall, A. Ayele, M. Wilks, A. Nowacki, and K. V. Cashman (2020). "Lower-Crustal Seismicity on the Eastern Border Faults of the Main Ethiopian Rift". *Journal of Geophysical Research: Solid Earth* 125(8). DOI: 10.1029/2020jb020030.

Le Corvec, N., T. Menand, and J. Lindsay (2013a). "Interaction of ascending magma with pre-existing crustal fractures in monogenetic basaltic volcanism: an experimental approach". *Journal of Geophysical Research: Solid Earth* 118(3), pages 968–984. DOI: 10.1002/jgrb.50142.

Le Corvec, N., K. B. Spörli, J. Rowland, and J. Lindsay (2013b). "Spatial distribution and alignments of volcanic centers: Clues to the formation of monogenetic volcanic fields". *Earth-Science Reviews* 124, pages 96–114. DOI: 10.1016/j.earscirev.2013.05.005.

Lutz, T. M. (1986). "An analysis of the orientations of large-scale crustal structures: A statistical approach based on areal distributions of pointlike features". *Journal of Geophysical Research* 91(B1), page 421. DOI: 10.1029/jb091ib01p00421.

Maccaferri, F., V. Acocella, and E. Rivalta (2015). "How the differential load induced by normal fault scarps controls the distribution of monogenic volcanism". *Geophysical Research Letters* 42(18), pages 7507–7512. DOI: 10.1002/2015gl065638.

Mackenzie, G. D., H. Thybo, and P. K. H. Maguire (2005). "Crustal velocity structure across the Main Ethiopian Rift: results from two-dimensional wide-angle seismic modelling". *Geophysical Journal International* 162(3), pages 994–1006. DOI: 10.1111/j.1365-246x.2005.02710.x.

Maestrelli, D., G. Corti, M. Bonini, D. Montanari, and F. Sani (2021). "Caldera collapse and tectonics along the Main Ethiopian Rift: reviewing possible relationships". *Comptes Rendus. Géoscience* 353(S2), pages 91–109. DOI: 10.5802/crgeos.63.

Maguire, P., G. Keller, S. Klemperer, G. Mackenzie, K. Keranen, S. Harder, B. O'Reilly, H. Thybo, L. Asfaw, M. Khan, and M. Amha (2006). "Crustal structure of the northern Main Ethiopian Rift from the EAGLE controlled-source survey; a snapshot of incipient lithospheric break-up". *Geological Society, London, Special Publications* 259(1), pages 269–292. DOI: 10.1144/gsl.sp.2006.259.01.21.

Mahood, G. A. (1984). "Pyroclastic rocks and calderas associated with strongly peralkaline magmatism". *Journal of Geophysical Research* 89(B10), page 8540. DOI: 10.1029/jb089ib10p08540.

Mazzarini, F., N. Le Corvec, I. Isola, and M. Favalli (2016). "Volcanic field elongation, vent distribution, and tectonic evolution of a continental rift: The Main Ethiopian Rift example". *Geosphere* 12(3), pages 706–720. DOI: 10.1130/ges01193.1.

Mohr, P., J. G. Mitchell, and R. G. H. Raynolds (1980). "Quaternary volcanism and faulting at O'A caldera, central ethiopian rift". *Bulletin Volcanologique* 43(1), pages 173–189. DOI: 10.1007/bf02597619.

Mohr, P. A. (1967). "Major Volcano–Tectonic Lineament in the Ethiopian Rift System". *Nature* 213(5077), pages 664–665. DOI: 10.1038/213664a0.

Molin, P. and G. Corti (2015). "Topography, river network and recent fault activity at the margins of the Central Main Ethiopian Rift (East Africa)". *Tectonophysics* 664, pages 67–82. DOI: 10.1016/j.tecto.2015.08.045.

Muluneh, A. A., S. Brune, F. Illsley-Kemp, G. Corti, D. Keir, A. Glerum, T. Kidane, and J. Mori (2020). "Mechanism for Deep Crustal Seismicity: Insight From Modeling of Deformation Processes at the Main Ethiopian Rift". *Geochemistry, Geophysics, Geosystems* 21(7). DOI: 10.1029/2020gc008935.

Muluneh, A. A., M. Cuffaro, and T. Kidane (2017). "Along-strike variation in deformation style inferred from kinematic reconstruction and strain rate analysis: A case study of the Ethiopian Rift". *Physics of the Earth and Planetary Interiors* 270, pages 176–182. DOI: 10.1016/j.pepi.2017.07.009.

Németh, K. (2010). "Monogenetic volcanic fields: Origin, sedimentary record, and relationship with polygenetic volcanism". *What Is a Volcano?* Edited by E. Cañón-Tapia and A. Szakács. Geological Society of America. DOI: 10.1130/2010.2470(04).

Paulsen, T. S. and T. J. Wilson (2010). "New criteria for systematic mapping and reliability assessment of monogenetic volcanic vent alignments and elongate volcanic vents for crustal stress analyses". *Tectonophysics* 482(1–4), pages 16–28. DOI: 10.1016/j.tecto.2009.08.025.

Rampey, M. L., C. Oppenheimer, D. M. Pyle, and G. Yirgu (2010). "Caldera-forming eruptions of the Quaternary Kone Volcanic Complex, Ethiopia". *Journal of African Earth Sciences* 58(1), pages 51–66. DOI: 10.1016/j.jafrearsci.2010.01.008.

Rooney, T. O., I. D. Bastow, and D. Keir (2011). "Insights into extensional processes during magma assisted rifting: Evidence from aligned scoria cones". *Journal of Volcanology and Geothermal Research* 201(1–4), pages 83–96. DOI: 10.1016/j.jvolgeores.2010.07.019.

Rooney, T. O., T. Furman, I. Bastow, D. Ayalew, and G. Yirgu (2007). "Lithospheric modification during crustal extension in the Main Ethiopian Rift". *Journal of Geophysical Research* 112(B10). DOI: 10.1029/2006jb004916.

Rubin, A. M. (1995). "Propagation of Magma-Filled Cracks". *Annual Review of Earth and Planetary Sciences* 23(1), pages 287–336. DOI: 10.1146/annurev.ea.23.050195.001443.

Samrock, F., A. V. Grayver, O. Bachmann, Ö. Karakas, and M. O. Saar (2021). "Integrated magnetotelluric and petrological analysis of felsic magma reservoirs: Insights from Ethiopian rift volcanoes". *Earth and Planetary Science Letters* 559, page 116765. DOI: 10.1016/j.epsl.2021.116765.

Samrock, F., A. V. Grayver, H. Eysteinsson, and M. O. Saar (2018). "Magnetotelluric Image of Transcrustal Magmatic System Beneath the Tulu Moye Geothermal Prospect in the Ethiopian Rift". *Geophysical Research Letters* 45(23). DOI: 10.1029/2018gl080333.

Saria, E., E. Calais, D. S. Stamps, D. Delvaux, and C. J. H. Hartnady (2014). "Present-day kinematics of the East African Rift". *Journal of Geophysical Research: Solid Earth* 119(4), pages 3584–3600. DOI: 10.1002/2013jb010901.

Siegburg, M., T. M. Gernon, J. M. Bull, D. Keir, D. N. Barfod, R. N. Taylor, B. Abebe, and A. Ayele (2018). "Geological evolution of the Boset-Bericha Volcanic Complex, Main Ethiopian Rift: 40Ar/39Ar evidence for episodic Pleistocene to Holocene volcanism". *Journal of Volcanology and Geothermal Research* 351, pages 115–133. DOI: 10.1016/j.jvolgeores.2017.12.014.

Tadesse, A. Z., D. Ayalew, R. Pik, G. Yirgu, and K. Fontijn (2019). "Magmatic evolution of the Boku Volcanic Complex, Main Ethiopian Rift". *Journal of African Earth Sciences* 149, pages 109–130. DOI: 10.1016/j.jafrearsci.2018.08.003.

Tadesse, A. Z., K. Fontijn, L. Caricchi, F. Bégué, S. Gudbrandsson, V. C. Smith, P. Gopon, V. Debaille, P. Laha, H. Terryn, G. Yirgu, and D. Ayalew (2023). "Pre-eruptive storage conditions and magmatic evolution of the Bora-Baricha-Tullu Moye volcanic system, Main Ethiopian Rift". *Lithos* 442-443, page 107088. DOI: 10.1016/j.lithos.2023.107088.

Tadesse, A. Z., K. Fontijn, A. A. Melaku, E. F. Gebru, V. C. Smith, E. Tomlinson, D. Barfod, P. Gopon, F. Bégué, L. Caricchi, P. Laha, H. Terryn, S. Gudbrandsson, G. Yirgu, and D. Ayalew (2022). "Eruption frequency and magnitude in a geothermally active continental rift: The Bora-Baricha-Tullu Moye volcanic complex, Main Ethiopian Rift". *Journal of Volcanology and Geothermal Research* 423, page 107471. DOI: 10.1016/j.jvolgeores.2022.107471.

Thomson, B. J. and N. P. Lang (2016). "Volcanic edifice alignment detection software in MATLAB: Test data and preliminary results for shield fields on Venus". *Computers amp; Geosciences* 93, pages 1–11. DOI: 10.1016/j.cageo.2016.04.012.

Tibaldi, A. (1995). "Morphology of pyroclastic cones and tectonics". *Journal of Geophysical Research: Solid Earth* 100(B12), pages 24521–24535. DOI: 10.1029/95jb02250.

Turdu, C. L., J.-J. Tiercelin, E. Gibert, Y. Travi, K.-E. Lezzar, J.-P. Richert, M. Massault, F. Gasse, R. Bonnefille, M. Decobert, B. Gensous, V. Jeudy, E. Tamrat, M. U. Mohammed, K. Martens, B. Atnafu, T. Chernet, D. Williamson, and M. Taieb (1999). "The Ziway–Shala lake basin system, Main Ethiopian Rift: Influence of volcanism, tectonics, and climatic forcing on basin formation and sedimentation". *Palaeogeography, Palaeoclimatology, Palaeoecology* 150(3-4), pages 135–177. DOI: 10.1016/s0031-0182(98)00220-x.

Vidal, C. M., K. Fontijn, C. S. Lane, A. Asrat, D. Barfod, E. L. Tomlinson, A. Piermattei, W. Hutchison, A. Z. Tadesse, G. Yirgu, A. Deino, Y. Moussallam, P. Mohr, F. Williams, T. A. Mather, D. M. Pyle, and C. Oppenheimer (2022). "Geochronology and glass geochemistry of major Pleistocene eruptions in the Main Ethiopian Rift: Towards a regional tephrostratigraphy". *Quaternary Science Reviews* 290, page 107601. DOI: 10.1016/j.quascirev.2022.107601.

WoldeGabriel, G., J. L. Aronson, and R. C. Walter (1990). "Geology, geochronology, and rift basin development in the central sector of the Main Ethiopia Rift". *Geological Society of America Bulletin* 102(4), pages 439–458. DOI: 10.1130/0016-7606(1990)102<0439:ggarbd>2.3.co;2.

Wolfenden, E., C. Ebinger, G. Yirgu, A. Deino, and D. Ayalew (2004). "Evolution of the northern Main Ethiopian rift: birth of a triple junction". *Earth and Planetary Science Letters* 224(1–2), pages 213–228. DOI: 10.1016/j.epsl.2004.04.022.